SAINT-PETERSBURG UNIVERSITY

Lozhkina Olga Aleksandrovna

Synthesis and Optical Properties of Halide Perovskites Single Crystals and Heterostructures

Scientific specialty
1.3.8. Condensed matter physics

Dissertation for the degree of
Candidate of Physical and Mathematical Sciences

Translation from Russian

Scientific advisor:
Candidate of Physical and Mathematical Sciences
Kapitonov Yury Vladimirovich

Saint Petersburg — 2023

Contents

Introduction

Modern semiconductor optics are based on covalent heterostructures, i.e. single crystals with artificial interfaces and low dimensional systems with specific optical properties. The epitaxial growth techniques used to produce such structures are vacuum, temperature and precursor sensitive, resulting in high energy consumption and cost. Finding new, cheaper and more efficient materials is a challenging task for semiconductor science.

The halide perovskites described in this work exhibit a unique combination of soft and cheap synthesis and outstanding optical properties: a lone pair on the valent s-orbital of the central metal atom, surrounded by a highly symmetric halogen environment, provides an unusual so-called defect tolerant band structure. The strong lowest direct optical transition determines an effective interaction with light, i.e. high optical absorption coefficient and quantum yield. Deep defects, which degrade the crystal quality, have a high energy of formation and therefore a low probability of formation.

The diversity of halide perovskite compositions and the availability of stable solid solutions in a wide range of concentrations make it possible to obtain materials with a given lattice constant and bandgap in the near infrared to ultraviolet range. Unlike traditional covalent semiconductors, the ionic nature of the materials is tolerant to significant lattice mismatch.

All this makes halide perovskites a promising candidate for cheaper and more effective optoelectronic devices. Therefore, the aim of this work is to investigate halide perovskites as a medium for semiconductor devices. The following **tasks** have been carried out:

1. Synthesis of halide perovskite single crystals $MAPbBr_3$, $CsPbBr_3$, $MAPbI_3$, $Cs_2BiAgBr_6$, and $CsPbBr_3$ with varied concentrations of Bi^{3+} impurity.
2. Study of halide perovskite single crystals photoluminescence at cryogenic temperatures.
3. Synthesis of a single crystal with a $MAPbBr_3/CsPbBr_3$ heterojunction and study of the optical properties of the heterojunction.

Scientific novelty:

The high optical quality of the synthesised halide perovskite single crystals provides well resolved phonon replica peaks in photoluminescence spectra. This is observed for the first time.

Low temperature Raman spectra have been recorded for the first time and correlated with the simulated phonon modes.

The first resolved low temperature photoluminescence spectrum has been obtained for $Cs_2BiAgBr_6$.

The first well-resolved low temperature photoluminescence spectra of bismuth doped $CsPbBr_3$ show bandgap stability in contrast to published data.

The first stable abrupt heterojunction between two halide perovskites has been synthesised and analysed.

Practical significance of the work. The work demonstrates the possibility of soft solution-based synthesis of ionic semiconductor structures. Specific examples of material compositions for low-dimensional systems for near infra-red to ultra-violet optical applications are suggested in the literature review.

Methodology and research methods. All reported samples were deposited from solutions. The composition and structure of the samples have been confirmed by energy dispersive X-ray analysis and backscattered electron diffraction. The main research method is low temperature photoluminescence, which provides information on the band gaps of the semiconductors and a quantitative characterization of their quality.

The main positions for the defense:

1. Exciton resonances with a linewidth of less than 1.5 meV are observed in the photoluminescence spectra of single crystals of halide perovskites $MAPbBr_3$, $CsPbBr_3$ and $MAPbI_3$ at cryogenic temperatures.
2. Exciton-phonon interaction in single crystals of halide perovskites $MAPbBr_3$, $CsPbBr_3$ and $MAPbI_3$ manifests itself in the form of phonon repetitions in the photoluminescence spectra.
3. The lowest interband transition in the lead-free double halide perovskite $Cs_2BiAgBr_6$ is indirect.
4. Heterovalent doping of $CsPbBr_3$ with Bi^{3+} ions does not affect the structure of the valence band and the band gap of the material.
5. Method for creating heterostructures with a $MAPbBr_3/CsPbBr_3$ heterojunction using liquid-phase growth of $MAPbBr_3$ on a single-crystal $CsPbBr_3$ seed.

Reliability of the results obtained is ensured by (1) the modern instrumentation involved in the work, (2) complementary studies results, (3) and agreement with published data.

Approbation. The main results of the work were presented at the following conferences:

1. Lozhkina, O. Low inhomogeneous broadening of excitonic resonance in $MAPbBr_3$ single crystal.*6th International Conference on Semiconductor Photochemistry*, 2017
2. Elizarov, M. et al. Synthesis and Characterization of Double Perovskites. *6th International Conference on Semiconductor Photochemistry*, 2017
3. Kapitonov, Yu. et al. Phonon replicas in $CsPbBr_3$ and $MAPbBr_3$ single crystals. *3rd International Conference on Perovskite Solar Cells and Optoelectronics*, 2017
4. Елизаров, М. В. и др. Влияния замещения свинца на висмут в перовските $CsPbBr_3$. *XIX Всероссийская молодежная конференция по физике полупроводников и наноструктур, полупроводниковой опто- и наноэлектронике*, 2017
5. Lozhkina, O. A. et al. Type-II heterojunction $MAPbBr_3/CH_3NH_3PbBr_3$. *5th International School and Conference «Saint-Petersburg OPEN 2018»*, 2018
6. Шиловских, В. В. и др. Применение метода EBSD для решения минералогических и кристаллографических задач. *Двадцать четвертая научная молодежная школа имени профессора В. В. Зайкова «Металлогения древних и современных океанов - 2018»*, 2018

Personal contribution. The synthesized samples and experimental results presented were obtained by the author personally or with her direct participation; the author participated in experiments, processing, discussion, analysis and interpretation of the experimental results.

This work was supported by Mega-grant № 14.Z50.31.0016 from the Government of the Russian Federation ”Creating the Laboratory of Photoactive Nanocomposite Materials” and Grant № 19-72-10034 from the Russian Science Foundation.

The work was carried out under the supervision of Kapitonov Yu. V. at the department of Photonics, St.Petersburg State University; samples were synthesised in the “Photoactive Nanocomposite Materials” laboratory, St.Petersburg State University; samples composition and structure were analyzed at the Research centres “Geomodel”, “Centre for Physical Methods of Surface Investigation”, “The Center of X-ray diffraction studies”, “Chemical Analysis and Materials Research Centre”, ”Centre for Extreme States of Materials and Constructions” and “Nanotechnology”; optical studies were performed at the Recearch Centre “Nanophotonics” and “Centre for Optical and Laser Materials Research” of the research park of St.Petersburg State University.

Publications. The main results are presented in 3 articles, including 3 of them published in Web of Science cited journals:

1. Lozhkina, O. A. et al. Low Inhomogeneous Broadening of Excitonic Resonance in $MAPbBr_3$ Single Crystals. *J. Phys. Chem. Lett.*, 2018, 9 (2), 302-305. DOI: 10.1021/acs.jpclett.7b02979.
2. Lozhkina, O. A. et al. Microstructural analysis and optical properties of the halide double perovskite $Cs_2BiAgBr_6$ single crystals. *Chem. Phys. Lett.*, 2018, 694, 18–22. DOI: 10.1016/j.cplett.2018.01.031.
3. Lozhkina, O. A. et al. Invalidity of Band-Gap Engineering Concept for Bi^{3+} Heterovalent Doping in $CsPbBr_3$ Halide Perovskite *J. Phys. Chem. Lett.*, 2018, 9 (18), 5408-5411. DOI: 10.1021/acs.jpclett.8b02178

All papers are presented in talk abstracts, a list of which is given in the previous paragraph.

The volume and structure of the work. The dissertation consists of introduction, four chapters, conclusions and two appendixes. The full volume of the thesis is 73 pages with 33 figures and 4 tables. The bibliograpy contains 0 positions.

Contents of the work. The first chapter is a literature review of the structure and physical properties of halide perovskites and the prediction of control of these properties by changing the chemical composition of the material. The second chapter presents a theoretical substantiation of the phenomenon of photoluminescence of semiconductor crystals and describes what information about the properties of the substance is reflected in the photoluminescence spectra. The third chapter lists the methods of synthesis and investigation of the studied materials. Finally, the fourth chapter presents the results of the study and provides a discussion.

Chapter 1. Literature review

1.1 Development of semiconductor electronics technology

The vast majority of modern electronic devices are made from semiconductor materials. The performance of semiconductor devices is based on electrons in solids. The properties of semiconductor materials are easily controlled by the addition of impurities; the conductivity of semiconductors is controlled by the introduction of a magnetic field, irradiation or mechanical deformation, making them excellent sensors successfully used in a wide variety of devices.

The development of semiconductor technology is primarily due to the invention of the bipolar transistor[1] in the work of W. Shockley and M. Sparks. The creation of the first demonstration transistor model required the development of melting, purification, semiconductor doping and layer growth technologies, but ultimately led to the explosive growth of semiconductor technology.

Later, J. Alferov developed semiconductor heterostructures - crystals with artificial interfaces between semiconductors of different composition and with different band gaps, which exhibit fundamentally new electronic phenomena in solids. A serious problem Alferov faced was finding suitable materials for heterostructures, since heterostructures require the simultaneous compatibility of thermal, electrical, crystal and bandgap properties[2]. A successful combination has been found in the form of AlAs-GaAs. Gallium arsenide is a direct-gap semiconductor (Figure 1.1c), stable in air and non-hygroscopic. It has higher electron mobility, radiation resistance and electric breakdown field strength than silicon. Its main feature is a stable ternary solution with aluminium arsenide over the whole concentration range (Figure 1.1b). The crystal lattice parameters of gallium arsenide and aluminium arsenide are very close, but the band gaps of these materials differ significantly(Figure 1.1a). These two factors make it possible to produce semiconductors with a given bandgap by controlling the composition of the ternary solution according to Vegard's law, and to produce high-quality heterojunctions of the two semiconductors due to the matching of their crystal structures, resulting in low mechanical stresses. In addition, at concentrations of aluminium arsenide not exceeding 45%, the ternary solution has a direct bandgap that allows effective interaction with light, so it is widely used in optoelectronics[3].

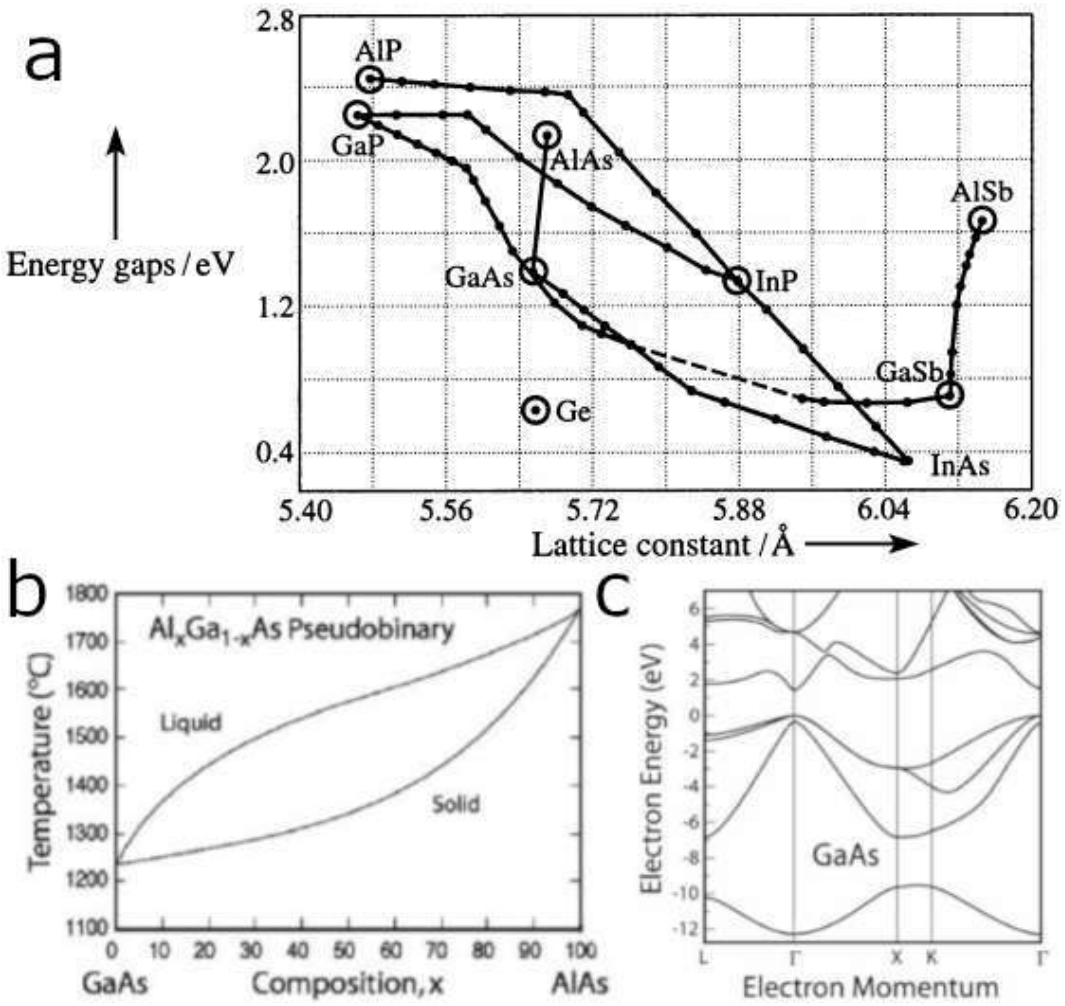

Figure 1.1 Bandgap and crystal structure properties of the AlAs-GaAs system: (a) the bandgap dependence on the crystal lattice parameters of covalent semiconductors A3B5[4], (b) the AlAs-GaAs phase diagram [3] and (c) the band structure of the solid solution $Al_xGa_{1-x}As$[3]

New fundamental physical phenomena of one-way and superinjection, electronic and optical confinement, and diagonal tunneling through heterojunctions were investigated with heterojunctions in the AlAs-GaAs system. These phenomena led to the development of fundamentally new devices: semiconductor lasers operating at room temperature, high-efficiency LEDs, solar cells, etc.

The phenomena of electronic and optical confinement attracted interest to the creation and study of double heterostructures with superfine layers demonstrating dimensional quantization, which raised again the problem of insufficient chemical purity and quality of the materials. Technology of epitaxy developed by J. Arthur and A. Cho[5] is one of the basic processes in semiconductor devices and integrated circuits technology today. Epitaxy is an oriented growth of one crystal on the surface of another one; it allows precisely defined layers with abrupt and distinct crystal lattice bound-

aries to be deposited. Molecular beam epitaxy is a method to obtain the highest quality heterostructures represents vacuum deposition of thin films on a crystalline substrate. The structures are grown in ultrahigh vacuum at specially selected temperatures which prevents mutual diffusion of different atoms to create heterointerfaces with an abrupt change in the chemical composition and electronic structure at the interface, but ensure effective surface diffusion to create a quality defect-free crystal structure. High requirements are also imposed on the quality of the crystal substrate and the purity of the molecular growth sources: defects that create deep levels are usually the centres of emission-free recombination and lead to a drastic decrease in the optical quality of the semiconductor crystal, the mobility and lifetime of carriers decrease dramatically with the formation of impurity levels in the band gap. Internal defects also determine the doping limit of the structure. Immediately during growth, the process parameters can be controlled by ellipsometry, electron diffraction, mass spectroscopy, and Auger spectroscopy. Thus, molecular beam epitaxy made it possible to create high-quality heterostructures with ultrathin layers, the study of which made it possible to reveal new quantum phenomena in solids, including two-dimensional electron gas, stepped density of states, quantum Hall effect, resonant tunneling in double barrier structures and superlattices, and others widely used in modern engineering - higher energy, higher power and efficient semiconductor lasers, two-dimensional electron gas transistors, resonant-tunnel diodes, electro-optical modulators[4].

The production of semiconductor heterostructures based devices includes, in addition to the growth of the heterostructure itself, the processes of lithography, deposition, etching, annealing, irradiation, etc. - The production of modern chips requires more than 300 processing steps and poses a significant health hazard, primarily due to the use of toxic substances (heavy metals, metal-organic precursors, hydrofluoric acid, organic solvents and others)[6].

A separate challenging technological problem is the gallium nitride semiconductor structures synthesis, which is used for the short-wave sources of radiation - in the green, blue and near-UV spectral regions[7].

In view of the above, the search for new semiconductor materials devoid of the drawbacks of currently used silicon, germanium, gallium arsenide and others, is an urgent task of modern physics. Such materials could be halide perovskites.

1.2 Halide perovskites

Lead and tin halide perovskites with the general formula ABX_3, where (where A^+ is a bulk alkali metal cation or an organic cation, B^{2+} is the central atom cation, X^- halogen anion) were actively investigated in the 1970s since the materials stood out among the corresponding simple halide salts by their coloration and high conductivity due to the highly symmetric environment of the central metal atom with a valent ns2 lone-pair, which usually distorts the symmetry[8–11].

Later these materials came into the lamelight as a photovoltaic material for solar cells after Miyazaki proposals published in 2006. In the work presented he used hybrid organic-inorganic perovskites $MAPbX_3$ ($MA^+ = CH_3NH_3{}^+$, $X^- = Br^-$) as dye in solar cells[12] while outstanding properties which the materials possess perfectly fit the photovoltaics needs, i. e. high optical absorption in the visible spectral region along with the direct bandgap and high mobility and mean free path lengths of carriers of both types. Solution processed single crystals exhibit carrier free paths up to 175 μм [13] and mobilities up to 25 $cm^2/V{\cdot}c$[14], concentration of traps as low as 10^9 per cm^3 [15] and radiative line width 1 meV[16]. The efficiency of radiation conversion in the most studied and popular at the moment $MAPbI_3$ based solar cell prototypes reached 22 %[17].

These properties together with the high quantum yield[18] are also in demand in photoelectronics. Recently have already been presented first prototypes of halide perovskite based lasers[19;20], light sources [21;22] and photodetectors[23–25].

1.2.1 Structure of halide perovskites

The extraordinary combination of mild chemical synthesis and outstanding optical properties of halide perovskites is due to the defect tolerance, which results from the unusual electronic structure of the materials.

$MAPbI_3$ is a nice example of halide perovskites. The compound has a high-temperature highly symmetric cubic structure. At elevated temperatures above 330 K the material has a P$m-3m$ spatial group: all lead cations are surrounded by an octahedra formed of six iodine anions and methylammonium cations occupy an intermediate twelve-coordinated position (½, ½, ½) between these octahedra (Figure 1.2)[26]. With decreasing temperature the crystal symmetry also decreases, it undergoes a transition to the tetragonal I4/mcm phase accompanied by a slight distortion of [PbI_6] octahedra around one of the axes. Further temperature decrease below 160 K leads to the [PbI_6] rotation and distortion of the structure into orthorhombic Pnma[27].

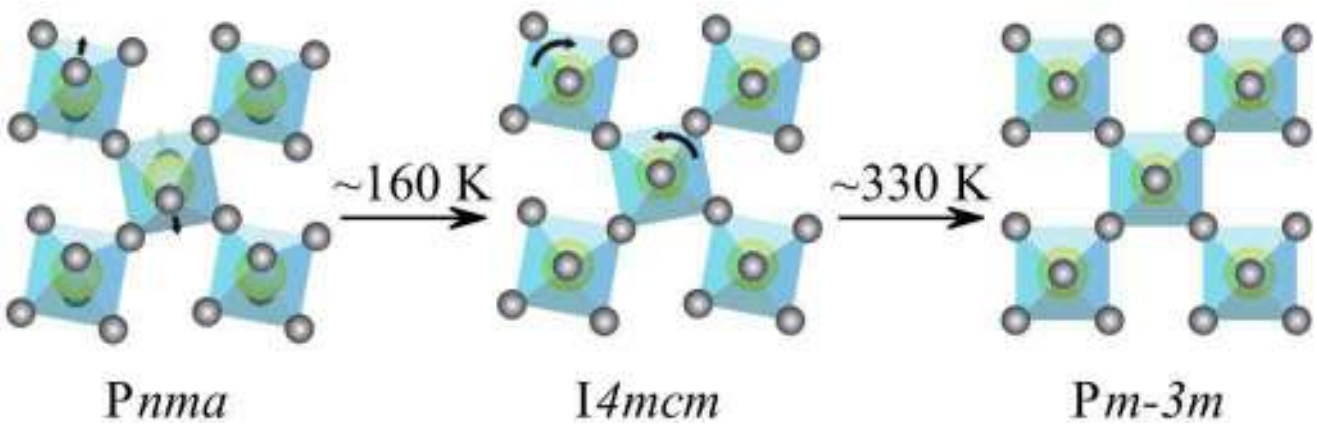

Figure 1.2 Schematic of $MAPbI_3$ phase transitions as temperature increases from distorted orthorhombic and tetragonal to highly symmetric cubic phase

The electron structure of the material is thus a result of lead and iodine atomic orbitals interaction in the [PbI_6] structure. The valence band maximum (VBM) is formed by anti-bonding Pb $6s$ and I $5p$ and the conduction band minimum (CBM) is formed by anti-bonding Pb $6p$ and I $5p$ orbitals (Figure 1.3)[28;29]. In such case deep defects influencing materials optical quality have high formation energies. This band structure significantly differs from conventional semiconductors, which valence bands consist mostly of binding orbitals. The p-orbitals are more localized and have a higher density of stated compared to the s-orbitals, which leads to high optical absorption in the case of halide perovskites.

The strong anti-bonding molecular orbital between Pb $6s$ and I $5p$ leads to low electron and hole masses and hence to long carrier free taths. The lone-pair on the central atom s-orbitals in the highly symmetric chemical environment results in the strong lowest direct $p - p$ transition in contrast to the weaker $p - s$ transition in the traditional photo-absorbing materials Cu(In,Ga)Se_2 and CdTe[30].

1.2.2 Tuning of halide perovskites properties

As mentioned above, the halide perovskites electronic structure is determined only by the interaction between the atomic orbitals of the cation B and the anion X, the cation A orbitals do not contribute to the VBM or CBM. However its nature still largely controls the shape of the [BX_6] octahedra and consequently the overlap between the B and X atomic orbitals and thus the perovskite properties. According to the experimental data[31;32] the perovskite bandgaps wide with the degree of the chemical bonding ionicity. Changes in the cation A size can lead both to a significant VBM shift with the bandgap narrowing caused by the B-X bonds shortening and decreasing the ionicity

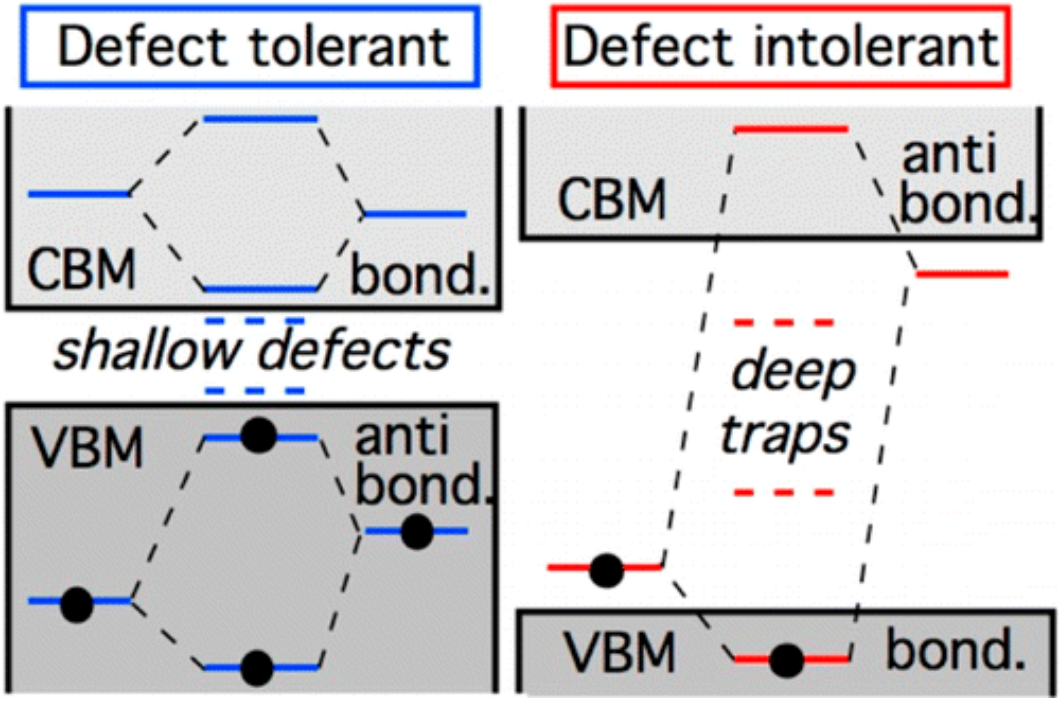

Figure 1.3 Molecular orbital schemes of defect tolerant and intolerant structures[30]

degree or the a slight widening of the bandgap by [BX_6] octahedra rotation causing the bonds elongation and distorting the crystal symmetry (Figure 1.4)[33;34]. The ionicity also rises with increasing cation B radius and decreasing anion X radius[35]. The valent orbital lone-pair is essential for defect tolerance and material optical properties, so the substitution of the B cation requires an element isoelectronic to lead, which can be germanium or tin or a heterovalent pair forming an elpasolith $Fm-3m$ structure In^{+}, Tl^{+}, Sb^{3+} and Bi^{3+} (Figure 1.5)[36]. According to simulations and experimental data, the lead substitution with homovalent (group 2 and 12) or heterovalent elements (groups 1, 3, 11, 13 and 15) leads most often to an indirect lowest transition or sometimes to a weak direct transition (Table 1)[37].

Table 1 Theoretically predicted data on the band gap structure of halide perovskites and the lowest electron transition on cation B substitution[37]

B^{2+}		$B^{+}B^{3+}$	Group 3	Group 13	Group 15
Group 2	Indirect	Group 1	Forbidden direct	Forbidden direct	Weak direct
Group 12	Indirect	Group 11	Indirect	Forbidden direct	Indirect
Group 12	Strong direct	Group 13	Weak direct	Indirect	Strong direct

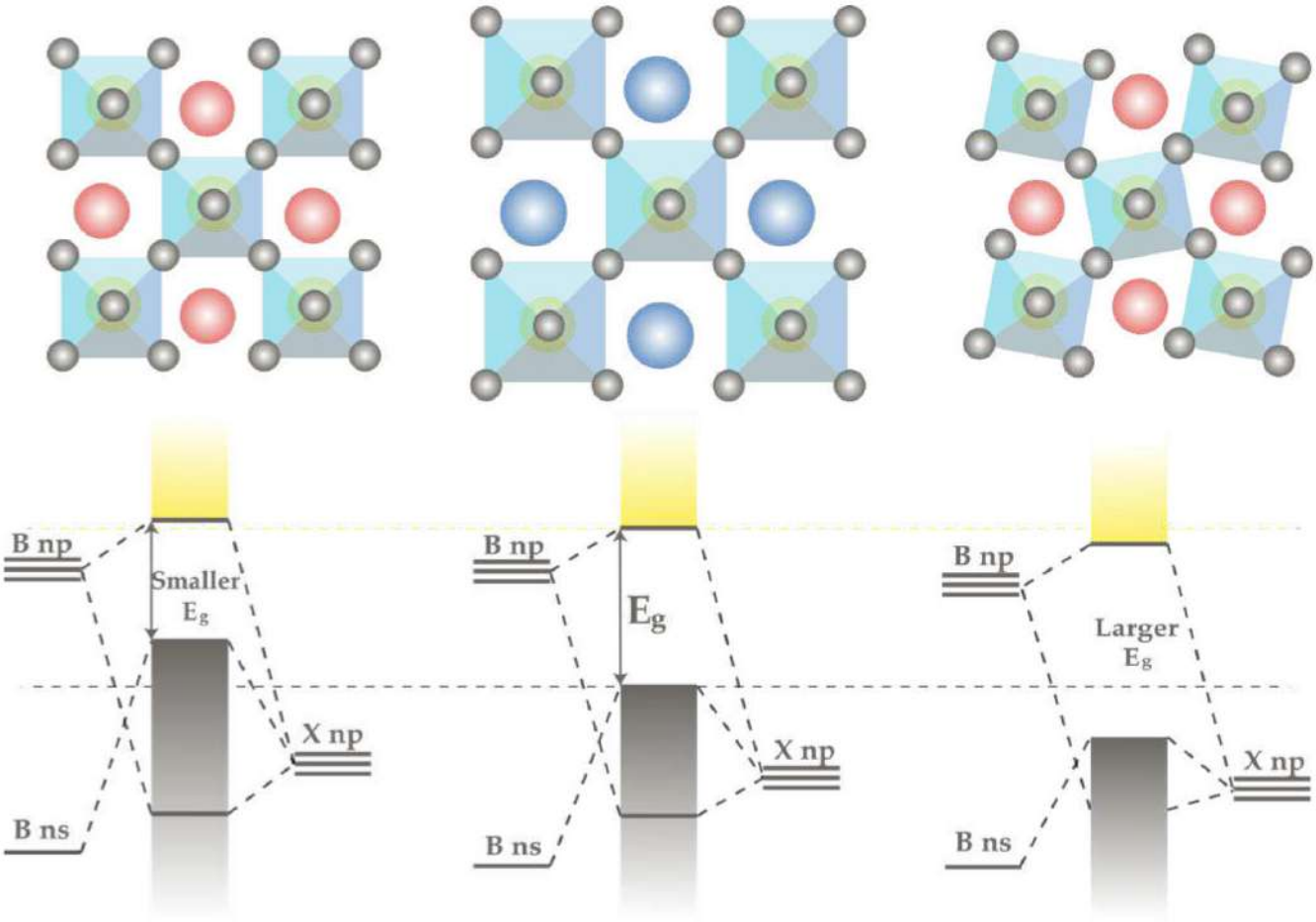

Figure 1.4 Schematic of the cation A radius reduction effect on the cubic halide perovskites bandgap (in the center)

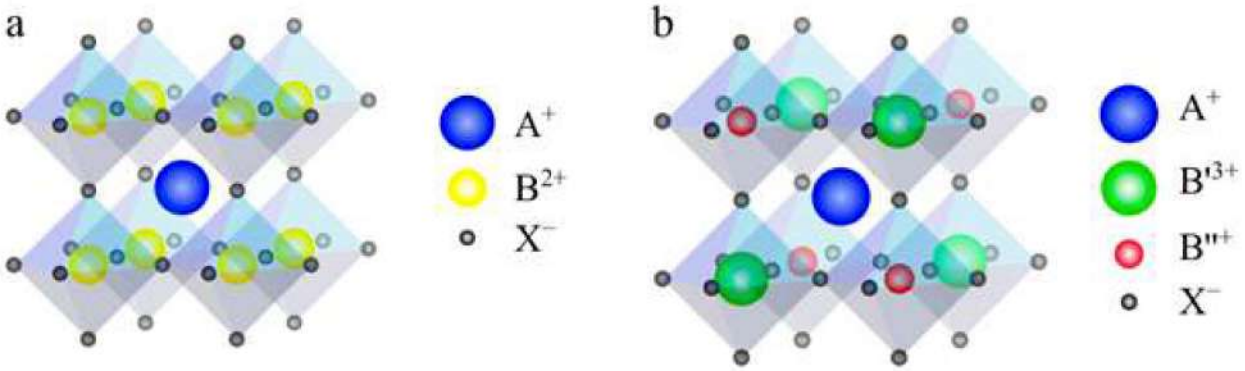

Figure 1.5 Scheme of heterovalent B cation substitution in halide perovskites, leading to the elpasolith structure

Transition metals have due to the *d*-compression have smaller sizes and only form stable cubic compounds with other small ions like Na^+, K^+, NH_4^+, F^- [38]. Physical and chemical properties of these materials are largely determined by partially filled localized *d*-orbitals and require a separate consideration.

Solid halide perovskite solutions formed by the B cation substitution exhibit an anomalous nonmonotonic change in the bandgap, which can be even narrower than that of individual pure compounds. According to Im et al.[39] this is caused by two competing factors: the spin-orbit interaction is strong for heavy atoms and causes the bandgap narrowing while the inpurity induced symmetry crystal lattice distortion widens the bandgap.

Anion partial substitution is used for gradual bandgap modulation, in this case the bandgap follows the Vegard's law[40;41]. The VBM density of states is formed mostly by halogen atoms and the anion substitution shifts the VBM position. The partial anion substitution was also demonstrated to improve the halide perovskite stability[42–44].

In conclusion, varying halide perovskite composition by partial ion substitution one can separately change material VBM, CBM and thus the bandgap within a small lattice distortion in a predictable way, which is extremely attractive for epitaxial growth of low dimensional systems.

1.2.3 Halide perovskites stability and the tolerance factor

The empirical octahedral and tolerance factors are used to estimate the halide perovskites stability. The general halide perovskites formula is ABX_3 (where A^+ is a large alkali or organic cation, B^{2+} is a lead or isoelectronic to lead central ion, X^- is a halogen anion; the ionic radii of mentioned ions are given in Table 2). The octahedral factor defines the six-coordinated B^{2+} and the anion sizes correspondence and is calculated via $\mu = r_B/r_X$. The octahedral factor value should exceed 0,442 for a stable octahedral environment.

The tolerance factor is defined as $\tau = \frac{r_A+r_X}{\sqrt{2}(r_B+r_X)}$ and equals 1 for the ideal perovskite structure, if the tolerance value lies in between 0,85 and 1,11 the perovskite structure is predicted to be stable, and for values in the range 0,9-1,0 cubic lattice is expected. Lower tolerance factor values correspond to distorted orthorhombic and tetragonal lattices, and increasing the A^+ size leads first to hexagonal lattice and further to two-dimensional layered structures[45;46].

Table 2 demonstrates the ionic radii or lead and isoelectronic to lead cations and pairs, halogens and large alkali or organic cations. Octahedral and tolerance factors were calculated for the radii given in the table (Appendix A), and according to the obtained values germanium, gallium, arsenic and antimony do not for stable halide perovskite compounds due to their small radii.

Table 2 Ionic radii of elements for calculating the octahedral and tolerance factors, including gallium, germanium, arsenic, and antimony, which have radii too small to form stable perovskite compounds, marked in red[47–51]

A^+ [Å] 12-coord.		B^+ [Å] 6-coord.		B^{2+} [Å] 6-coord.		B^{3+} [Å] 6-coord.		X^- [Å] 6-coord.	
Rb^+	1,72	Ga^+	1,13	Ge^{2+}	0,73	As^{3+}	0,58	Cl^-	1,81
Cs^+	1,88	In^+	1,32	Sn^{2-}	1,02	Sb^{3-}	0,76	Br^-	1,96
MA^+	2,17	Tl^+	1,50	Pb^{2+}	1,19	Bi^{3+}	1,03	I^-	2,20
FA^+	2,53								

A number of lead halide perovskites with chlorine, bromine or iodine as the X-site anions and rubidium, cesium, methylammonium and formamidium as the A-site cations have been synthesized[52–56]. Bulk organic cations in A+ position produces reduced-dimentional perovskites with special optical properties[57;58].

Complicated synthesis and low stability of mentioned elements in the given oxidation stated is a serious problem reducing the halide perovskites composition variety: isolelectronic to lead cations Ge^{2+}, Sn^{2+} as well as Ga^+ and In^+ are extremely unstable towards oxidation[59–62].

Tin(II) compounds synthesis must be performed in the strong reducing agents presence and the product is often unstable even in the inert atmosphere[63]. Nevertheless, the synthesis and carackterization of several tin halide perovskites has been reported[64–66]. In [67] the possibility to tune the halide perovskite bandgap with lead substitution with tin was demonstrated.

Despite the small germanium ionic radius and octahedral and tolerance factors values outside the stability zone, various Ge^{2+} compounds with brutto formula ABX_3 and distorted lattices have been synthesized and studied[68–70]. The theoretical work by Ju et al.[71] proposed a mixed $RbSn_{0.5}Ge_{0.5}I_3$ as a potentially stable material.

Nowadays the only reported double perovskite of high optical quality comparable with $MAPbI_3$ is $(MA)_2TlBiBr_6$ [72], but due to the high thallium toxicity it does not find practical application. The work by Volonakis et al.[73] demonstrated increasing stability with respect to oxidation with increasing A^+ ionic radius and the $(Cs/MA/FA)_2InBiBr_6$ stability was theorized. Bismuth partial substitution by antimony atoms is also possible[74] and leads to the bandgap narrowing.

1.2.4 Halide perovskites point defects

Defects of semiconductor crystals significantly affect their optical and electrical properties. Donor or acceptor defects change the carrier concentrations, lattice defects serve as light-emitting or non-emitting recombination centres, reducing the main transition quantum yield and the carriers lifetime.

This leads to an extensive study on halide perovskites defects nature using first-principles calculations. As the defect tolerance is the main halide perovskite feature rising from their unusual band structure, point defects with low formation energies only form shallow levels in the bandgap, while deep defects have high formation energy. Halide perovskites can controllably demonstrate good intrinsic p- or n-type conductivity depending on the growth conditions, i. e. the halide source chemical potential since the main donor and acceptor defects have close formation energies. Among the possible ABX_3 point defects there are three vacancies (V_A, V_B, V_X), three interstitial defects (A_i, B_i, X_i) and six antistructure defects (A_B, B_A, A_X, B_X, X_A и X_B).

Simulations on $MAPbBr_3$ reveal that the donor defects formation energies are higher and their formation probability is therefore lower than that of acceptor defects, and thus the intrinsic p-type conductivity is characteristic for the material. The acceptor levels are mostly located in the valence band, except for Br_{Pb} which forms a shallow level in the bandgap. Donor defects mainly form deep levels with high formation energy, except for Pb_{MA}, which forms a shallow level (Figure 1.6a)[75].

Calculations for $CsPbBr_3$ show that V_{Cs}, V_{Pb}, Cs_{Pb} and Br_{Cs} form shallow acceptor levels, while VBr and PbVs are donor levels (≤100 meV) with low formation energy; Br_{Pb} forms a deep acceptor level, but its formation energy is high (Figure 1.6b)[76].

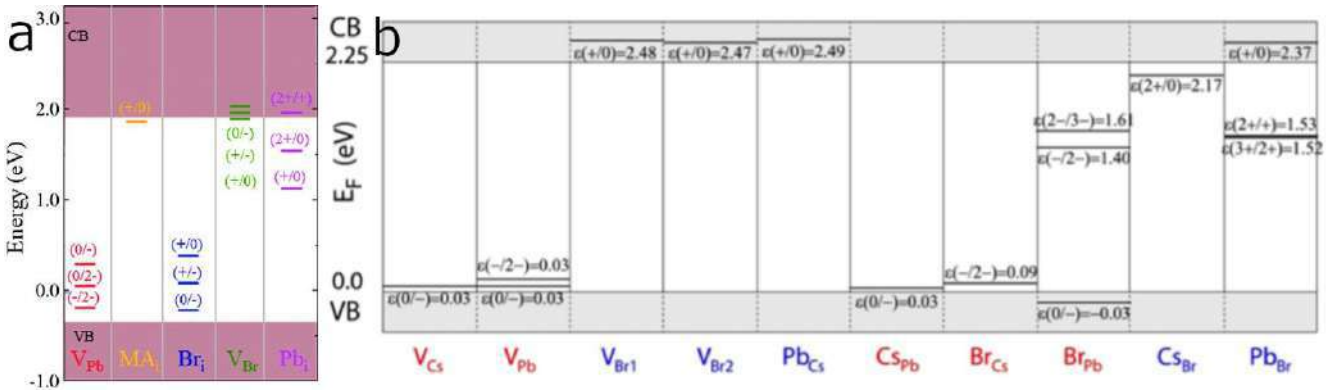

Figure 1.6 First-principles calculations on the point defects in (a) $MAPbBr_3$ [77] and (b) $CsPbBr_3$[76] halide perovskites

In the $MAPbI_3$ case defects with low formation energies MA_i, V_{Pb}, MA_{Pb}, I_i, V_I and V_{MA} form shallow levels within 50 neV above VBM or below CBM. I_{Pb}, I_{MA}, Pb_i and Pb_I forming deep levels also have high formation energies (Figure 1.7) [78].

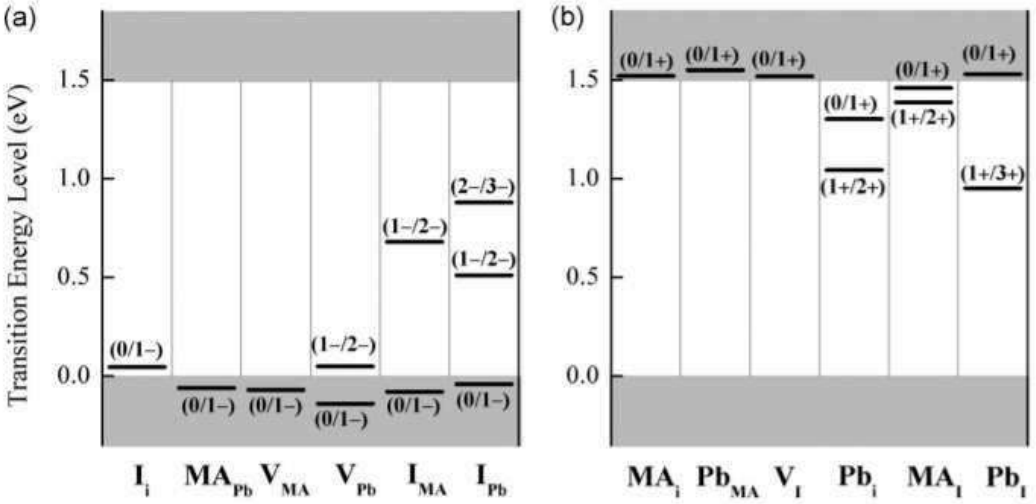

Figure 1.7 Данные первопринципных расчетов об энергетическом положении точечных дефектов галогенидного перовскита $MAPbI_3$[78]

1.2.5 Electron doping of halide perovskites

Electron doping is widely used in semiconductor engineering to control the electrical properties of a semiconductor. The introduction of impurities can significantly increase the concentration of carriers of a given type and, consequently, the conductivity. A number of papers investigating the possibility of electron doping of halide perovskites with heterovalent cations [79–84] are presented. The theoretical work by Abdelhady et al.[85] shows that the introduction of heterovalent bismuth and thallium impurities in $MAPbI_3$ does not change the band structure of the semiconductor, leading only to a shift of the Fermi level. Among the dopants of greatest interest is bismuth, which has the same electronic structure of the valence shell ns^2np^0 as lead, in addition, being in a highly symmetric chemical environment, it has a relatively narrow bandgap widths[86], which is important for optical applications of doped perovskites. Bismuth is stable, safe and has an ionic radius close to that of lead (1.03 and 1.19 Å, respectively). Several works [84;87–91] study bismuth-doped halide perovskites synthesized from solutions. The concentration of bismuth in the products depends linearly in the interval studied on its concentration in the mother liquor - bismuth is reluctant to be incorporated into the crystal lattice, but even its small concentrations (on the order of 10^{17} Bi atoms per cm^3) dramatically change the color of the obtained crystals and increases the conductivity,

transforming halide perovskites from intrinsic p-type semiconductors[15] to impurity n-type ones (Figure 1.8).

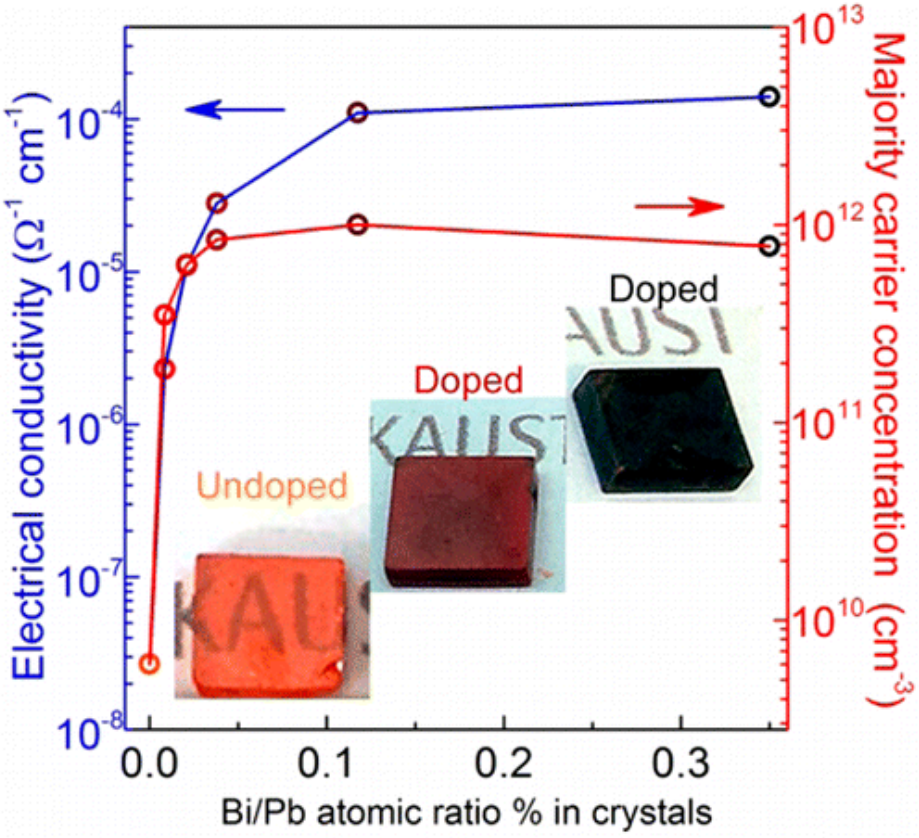

Figure 1.8 Conductivity and concentration of main charge carriers in bismuth doped $MAPbBr_3$ single crystals[84]

Several works[84;87;88] based on this color change from the optical absorption data draw conclusions about a significant narrowing of the band gap width of materials with the introduction of bismuth additives were made. However, other authors[90;91] indicated a misinterpretation of the obtained spectra - the absorption shift to the red region is caused by a violation of the crystal order of the materials, which is expressed in the absorption spectra in the form of Urbach tails. The constancy of the bandgap width was shown by indirect spectroscopic ellipsometry, as well as by photoluminescence and reflection spectroscopy. Some deterioration of the optical properties of the material, manifested in the low-temperature photoluminescence spectra, is caused by the formation of internal microstresses on which inelastic exciton scattering occurs and by the formation of deep traps on bismuth atoms embedded in the crystal structure.

1.2.6 Halide perovskites heterostructures synthesis

Unlike the covalent semiconductors mentioned above, perovskites are much less demanding to growth conditions: single crystals and monocrystalline films of high optical quality are obtained by melt growth, solution deposition, or vapor deposition[92–99]. Cesium trihalogenostannate[92;93] is successfully obtained as bulk single crystals, methylammonium and formamidium[94] and trihalogen-plumbates in a wide range of cation and anion substitutions[95–99].

The ionic nature of the compounds makes it possible to build up materials with markedly different crystal lattice constants and symmetries on each other or on numerous industrial alkali metal halide substrates that have a suitable cubic structure, a large range of crystal lattice constants and are transparent in a wide range of radiation without distortion of structure due to chemical wetted surface[99]. The sputtering of these salts on top of the finished structures can also protect perovskites, known to have low resistance to oxygen and air moisture. Thus, the use of perovskites to produce heterostructures should result in materials of close quality with much less time, energy, and finance. However, one should keep in mind the high mobility of halogen ions, which does not allow creating a sharp crystal boundary with different anions in the composition[100].

Heterostructures based on halide perovskites with heterointerfaces formed by materials with different anions were synthesized by ion exchange methods in the systems $MAPbCl_3$/$MAPbBr_3$ and $MAPbBr_3$/$MAPbI_3$[101;102] and laser-initiated spinodal decay of the mixed compounds $CsPbB_{3-x}I_x$ and $MAPbB_{3-x}I_x$ [103]. In both cases there is no stable abrupt boundary between the materials.

Epitaxial single-crystal $MAPbI_3$ films of 200-300 nm thickness on a KCl substrate were synthesized by spin-coating[104].

In the work by Chen et al.[99] the single crystal films of $CsSnBr_3$ and $CsPbBr_3$ with different thickness on NaCl substrate are presented. In the work by Wang et al.[105] the 5-200 nm growth of $CsSnBr_3$ monocrystalline films on a NaCl substrate was performed by reactive vapor deposition with $in\ situ$ control by fast electron diffraction with atomic precision. The obtained films show a clear quantum shift with respect to the bulk material.

Epitaxial deposition of $CsPbBr_3$ thin films on CaF_2 and NaCl substrates is described in the work of Jiang et al.[106]

Literature data concerning the crystallographic data and bandgap widths of perovskites of different compositions are, unfortunately, quite contradictory due to the

difficulties of synthesis and stabilization of substances and study in the overwhelming majority of powders and nanocrystals of the studied materials. An attempt to summarize the available experimental data is presented in Figure 1.9.

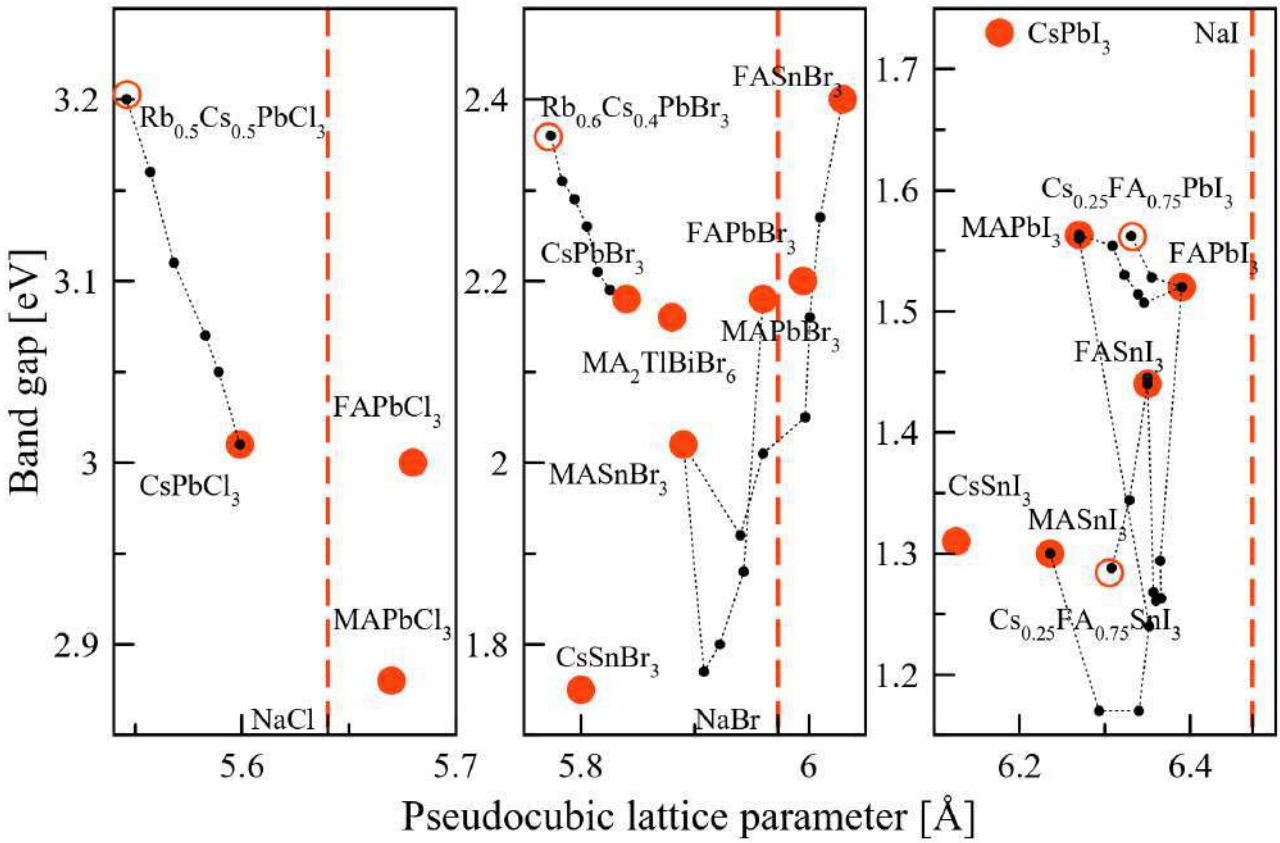

Figure 1.9 Bandgaps vs. cubic (for P$m-3m$ and F$m-3m$ structures) or pseudocubic (for P$4mm$, A$mm2$, I$4mcm$ and Pnma structures) crystal cell parameters. The red dotted line indicates the cell parameters of NaCl, NaBr, and NaI, which can serve as a substrate or cap layer, and the black dotted line indicates the data on solid solutions of these compounds. The graph is based on a number of publications[33;54;55;66;67;72;92;95;107–111]

As can be seen in the image, the crystal lattices of sodium halide perovskites are close in size to those of halide perovskites, so they can serve as substrates for growth or as a protective layer against oxidation and hydrolysis.

Chloride perovskites occupy a narrow spectral range in the near-UV range, so they are of little use for building heterostructures, and of little interest for optoelectronic applications. Bromide and iodide perovskites have a broader spectral distribution in the more convenient visible and infrared spectral regions.

Solid solutions of anion and cation A substitution obey Vegard's law well. Non-monotonic nonlinear dependences are observed for solid solutions of cation B sub-

stitution and allow modulation of the band gap width in an even wider range - to obtain materials more narrow-gap than individual components.

In the case of gallium-aluminum arsenide-based heterostructures, the energy gap between the bandgaps of adjacent materials does not exceed 300 meV. Specific examples of materials for making heterostructures based on halide perovskites in the case of bromides could be in the case of bromide $CsSnBr_3$ pairs (a=5.8 Å, E_g=1.75 eV) and $Rb_{0.3}Cs_{0.7}PbBr_3$ (a=5.81 Å, E_g=2.26 eV), and in the case of iodides $MASn_{0.5}Pb_{0.5}I_3$ (a=6, 34 Å, E_g=1.17 eV) and $MA_{0.4}FA_{0.6}PbI_3$ (a=6.34 Å, E_g=1.51 eV) or $Cs_{0.15}FA_{0.85}PbI_3$(a=6.36 Å, E_g=1.53 eV).

Thus, halogenide perovskites, being ionic semiconductors with a defect-tolerant band structure, are not demanding to synthesis conditions and have outstanding optical and electrical properties, which are in demand for the design of semiconductor devices. It is possible to control the type and magnitude of the electrical conductivity of the material, as well as to separately control the CBM, VBM, wide bandgap and lattice constant positions, which is extremely attractive for epitaxial growth of heterostructures and obtaining systems with reduced dimensionality.

The above data are of interest with regard to the effect of changes in the composition of halide perovskites on their optical properties, which leads us to formulate the following tasks:

1. The study on a hybrid organic-inorganic halide perovskite $MAPbBr_3$ single crystal optical properties.
2. The study on the cation, the anion and the central atom substitution.
3. The study on electrical properties tuning via electron doping.
4. And a halide perovskite semiconductor heterostructure synthesis and the study on its optical properties.

Chapter 2. Theoretical part

2.1 Semiconductor band structure

A semiconductor crystal can be described as a set of one-electron systems ordered into a periodic crystal structure. Using the free-electron approximation, the electron-electron interaction can be disregarded, and the electron-state interaction can be represented as a periodic potential $V_{eff}(r)$ with period L. Thus, the Schrödinger equation takes the form

$$H_0\psi(r) = [\frac{-\hbar^2}{2m}\nabla^2 + V_{eff}(r)]\psi(r) = E\psi(r). \tag{2.1}$$

According to Bloch theorem, the wave function of an electron in a semiconductor as a consequence of a periodic potential is a modulated plane wave:

$$\psi(r) = u_k(r) \cdot e^{ik}, \tag{2.2}$$

where u_k is the periodicity function of the crystal lattice. Solving equation (2.1) of the wave function form (2.2) shows that the eigenvalues lie in two resolved energy zones: valence and conduction. The relation between the energy of each resolved state and its wave vector k is called the dispersion law $E(k)$ for the valence band (Figure 2.1):

$$E_v = -\frac{\hbar^2 k^2}{2m_v} \tag{2.3}$$

and for the conduction band:

$$E_c = E_g + \frac{\hbar^2 k^2}{2m_c}, \tag{2.4}$$

where $m_{v,c}$ are the effective masses of the electron. Electrons obey Fermi-Dirac statistics, and the probability of the semiconductor energy level E population in thermal equilibrium

$$f(E) = \frac{1}{1 + e^{\frac{E-E_F}{k_B T}}}, \tag{2.5}$$

where k_B is the Boltzmann constant and E_F is the Fermi level.

When light is absorbed, electrons can be thrown from the valence band into the conduction band, leaving a hole (electron vacancy). Intraband relaxation-thermalization is a fast process compared to interband relaxation, and quasi-thermal equilibrium is established in the bands (Figure 2.2). The density of states is defined

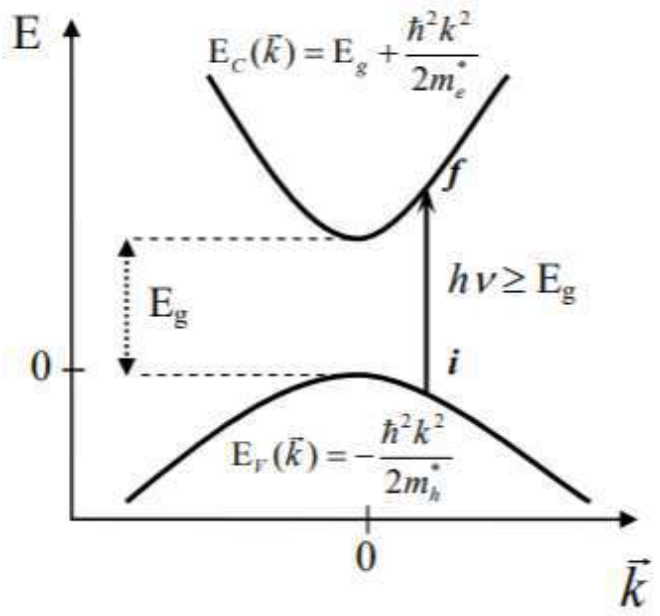

Figure 2.1 Dispersion law for an infinite semiconductor crystal[112]

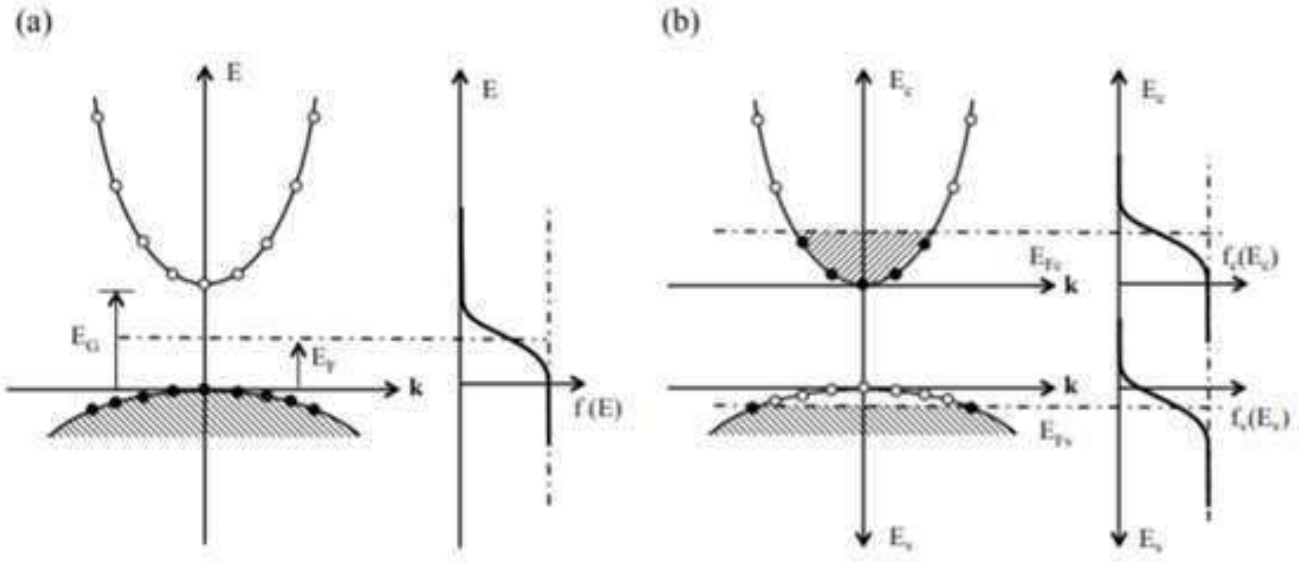

Figure 2.2 Semiconductor energy bands population at thermal (a) and quasi-thermal (b) equilibrium

as the ratio of the available volume to the volume of one state and takes the form as a function of energy for the parabolic dispersion law:

$$\rho(E) = \frac{1}{2\pi^2}\left(\frac{2m}{\hbar^2}\right)^{3/2}\sqrt{E}, \tag{2.6}$$

that is, it has a root form near the edge of the band.

2.1.1 Impurities and defects

Impurities and defects change the energy spectrum of a semiconductor: if the impurity and defect concentration $\rho_d \ll \left(\frac{1}{r_0}\right)^3, \left(\frac{1}{a_B}\right)^3$, where r_0 and a_B are the screening and Bohr radius of impurity respectively, a narrow energy level is formed in the band gap. If there is a Coulomb interaction between defects at $\rho_d \approx \left(\frac{1}{r_0}\right)^3$, a classical impurity level broadening occurs. If there is charge tunneling between the impurity levels at $\rho_d \approx \left(\frac{1}{a_B}\right)^3$, an impurity band is formed. Quantum broadening depends primarily on the dielectric permittivity of the semiconductor and can be observed even at low concentrations of impurity. At high doping concentrations $\rho_d > \left(\frac{1}{a_B}\right)^3$ the impurity bands combine with the eigenstate bands to form Urbach tails.

2.1.2 Optical absorption

According to Fermi's golden rule, when perturbed by an electromagnetic wave in the dipole approximation $H' = -eE_0 e^{i(k_{opt}\cdot r - 2\pi\nu t)} \cdot r$ transition probability between two states of a quantum system E_1 and E_2:

$$W_{1\to 2} = \frac{2\pi}{\hbar}|\langle 1|H'|2\rangle|^2\rho = \frac{\pi^2}{\hbar^2}\left|\int \psi_2 * \left(-er \cdot E_0 e^{i(k_{opt}\cdot r)}\psi_1 dV\right)\right|^2 \delta\left(\nu - \frac{(E_2 - E_1)}{h}\right) \tag{2.7}$$

In this case, the transition probability is not zero only if:

- photon energy equals the transition energy;
- вwave vectors obey the relation k_2=$k_{opt} + k_1$, that is, $k_2 = k_1$ given the small value of k_{opt}.

Taking into account the conservation of energy and quasi-momentum,

$$E_0 = E_g + \frac{\hbar^2 k^2}{2m}, \tag{2.8}$$

and the semiconductor optical absorption coefficient at $E_g \ll T$

$$\alpha(\nu) = \frac{\pi^3\nu}{\eta\varepsilon_0 ch^3}\frac{\mu^2}{3}2m^{3/2}\sqrt{h\nu - E_g}, \tag{2.9}$$

where μ is the transition matrix element.

In the presence of Urbach tails, the absorption spectrum near the edge of the band gap has an exponential dependence:

$$\alpha(\nu) = \alpha_0 e^{\frac{h\nu - E_g}{k_B T}}. \tag{2.10}$$

2.2 Excitons in semiconductors

The electron-hole pairs formed by radiation absorption can bind due to the Coulomb interaction, forming Vanier-Mott excitons, weakly bound collective excitations of the crystal. Solving the Schrödinger equation for the electron and hole

$$\left[\frac{\overline{h}^2}{2m_e}\nabla_e^2 - \frac{\overline{h}^2}{2m_h}\nabla_h^2 - \frac{e^2}{\eta\varepsilon|r_e - r_h|}\right]\Psi(r_e,r_h) = E\Psi(r_e,r_h), \tag{2.11}$$

we get for the corresponding variables $\Psi(R,r) = \varphi(R)\psi(r)$, $R = \frac{m_e r_e + m_h r_h}{m_e + m_h}$, $r = r_e - r_h$, $E = E_1 + E_2$ the equation for the free motion of a particle

$$\frac{-\overline{h}^2}{2(m_e + m_h)}\nabla_R^2\varphi(R) = E_1\varphi(R) \tag{2.12}$$

and the hydrogen-like particle equation

$$\frac{-\overline{h}^2 m_e m_h}{2(m_e + m_h)}\nabla_r^2\psi(r) - \frac{e^2}{\eta\varepsilon r}\psi(r) = E_2\psi(r), \tag{2.13}$$

from which the radius of the exciton:

$$r_e x = \frac{\eta\varepsilon\overline{h}^2}{m_r e^2} \tag{2.14}$$

and exciton level energies:

$$E_n = \frac{e^2}{2\eta\varepsilon r_{ex}}\frac{1}{n^2} = \frac{E_b}{n^2}. \tag{2.15}$$

Excitons in bulk semiconductors have low exciton binding energies E_b relative to the energy of thermal motion at room temperature, but at low temperatures the edge of the semiconductor's own absorption is largely determined by exciton effects: absorption of photons occurs with energy $h\nu \geqslant E_g - E_b$(Figure 2.3).

2.2.1 Excitonic photoluminescence

The excess energy caused by optical absorption is emitted in the form of photoluminescence during recombination of nonequilibrium carriers. Luminescence during interband recombination is not an inverse to the absorption process, because only thermally excited charge carriers participate in the luminescence process, so the luminescence spectrum is a narrow line.

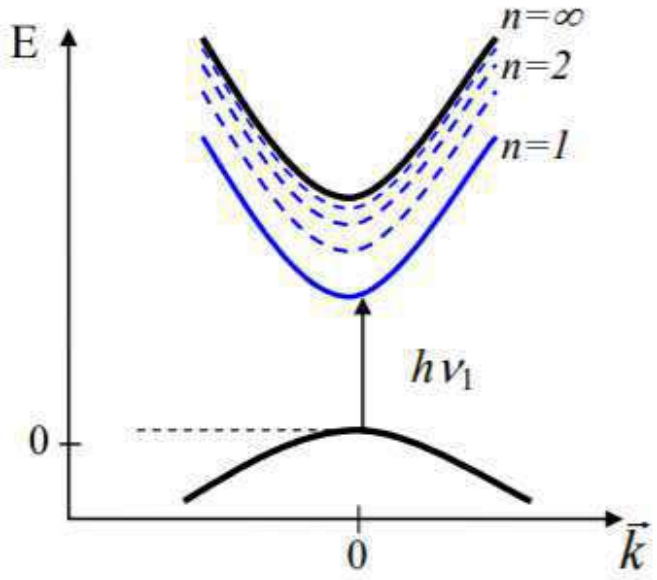

Figure 2.3 Exciton dispersion law in a Semiconductor[112]

Radiative annihilation of a free exciton in a direct bandgap semiconductor emits a photon with energy $h\nu - E_g - \frac{E_b}{n^2}$; if one of the carriers is localized on a defect, the emission during free exciton recombination is shifted to the red region (recombination at Schockley-Reed-Hall traps).

The interband recombination rate for semiconductors at thermal equilibrium can be represented as

$$I_{r_0} = \frac{\int_0^{\inf} 8\pi n_0^2 \nu \alpha_g(\nu) d\nu}{c^2 \left[e^{\frac{h\nu}{k_b T}} - 1 \right]}, \tag{2.16}$$

where $\alpha_g(\nu)$ is the interband absorption coefficient and n_0 is the refractive index. When deviating from the state of equilibrium

$$I_r = \frac{(n + \Delta n)(p + \Delta p)}{np} I_{r_0}, \tag{2.17}$$

where n and p are the equilibrium concentrations of electrons and holes, from which the emissive recombination time determines the natural width of the photoluminescence line,

$$\tau \approx I_{r_0} \frac{np}{n + p}. \tag{2.18}$$

The photoluminescence line width is determined by the times of radiation and non-radiation attenuation. The first quantity describes scattering on crystal lattice vibrations, its contribution depends on temperature and near 0 K in the region of scattering only on acoustic phonons the line width according to the Lee and Koteles theory[113] depends linearly on temperature, and extrapolation to 0 K gives the value of non-radiation

attenuation time, characterizing the material quality. In the case of indirect-gap semiconductors, radiative recombination of the free exciton is possible only with phonons, which is due to the law of conservation of quasimomentum. Due to the electron-phonon interaction, exciton annihilation is accompanied by phonon emission, which can lead to the appearance of additional phonon recombination bands that are separated from the exciton line by the energy of the corresponding phonons.

2.2.2 Phonon replicas in photoluminescence spectra

Outside the region of resonant exciton absorption in the luminescence spectra, lines caused bypartial energy transfer between excitons and crystal lattice vibrations with phonon formation or absorption are observed . The position of the phonon replicas is determined by the energy conservation law $\omega_{ph} = \omega_{exc} - m\omega_{LO}$, where m is an integer. The intensity of the phonon replica depends on the exciton-phonon interaction function, which in turn is determined by the radii of the exciton and phonon, determined by its wave line, and the ratio of the effective masses of the electron and hole[114].

Chapter 3. Sample synthesis and methods of investigation

3.1 Synthesis and sample preparation

A list of the reagents and materials used for the synthesis is given in Appendix B.

3.1.1 Synthesis of $MAPbBr_3$ single crystals

The synthesis was carried out according to the method described in the paper by Abdelhady et al.[84]. Crystallization was carried out from a solution containing 1.2 M MABr and 1 M $PbBr_2$, an excess of MABr being necessary to avoid precipitation of lead bromide; for this purpose, 1.344 g MABr and 3.670 g $PbBr_2$ were placed in a 10 ml measuring flask, weighted on analytical scales with 10^{-3} g precision. The powders were then poured over to the line with dimethylformamide and stirred until dissolved. The obtained solution was filtered with a cellulose filter and placed in a 20 mL beaker. The sealed beaker was heated in a water bath to 80°C and incubated for 4 hours. The formed orange single crystals were removed from the reaction mixture and air dried until the solvent evaporated, then stored in a desiccator. All surface analyses (EDX, EBSD, PL) were performed on the freshly cleaved surfaces.

3.1.2 Synthesis of Bi-doped $CsPbBr_3$ single crystals

The synthesis was carried out according to the method described in the paper by Ding et al.[115]. Crystallization was carried out from a solution containing 1 M CsBr and 1 M $PbBr_2$, the lack of cesium bromide is necessary to avoid precipitation of the side phase Cs_4PbBr_6; for this purpose 2.128 g CsBr and 3.670 g $PbBr_2$ were placed in a measuring flask for 10 ml, weighed on analytical scales with an accuracy of 10^{-3} g. In order to obtain doped samples a portion of $PbBr_2$ was substituted with $BiBr_3$ in appropriate proportions (Table 3), for this purpose a 0.3 M $BiBr_3$ solution was obtained, the given volume of which was placed using a adjustable micropipette for 10-100 or 100-1000 μl into the flask together with bromide powders.

The powders were then poured over to the line with dimethylsulfoxide and stirred until dissolved. The obtained solution was filtered with a cellulose filter and placed in a 20 ml beaker. The beaker was sealed with Parafilm film, which had a small hole made with a needle. The beaker with the reaction mixture was placed in a 100 ml beaker containing 20 ml of 20% ethanol solution in water. The container was heated to

Table 3 Quantities of reagents for the synthesis of bismuth-doped $CsPbBr_3$ single crystals

Bi^{3+}/Pb^{2+} in solution	m_{CsBr} [g]	m_{CsBr} [g]	V_{BiBr_3} [ml]
0 %	2,128	3,670	0
0,025 %	2,128	3,670	0,01
0,05%	2,128	3,670	0,02
0,5 %	2,128	3,670	0,20
1 %	2,128	3,633	0,40
2 %	2,128	3,597	0,80
5 %	2,128	3,487	2,00

40°C on a hotplate and incubated for two days. The resulting yellow-orange to black single crystals were taken out of the reaction mixture and air dried until the solvent evaporated, then stored in a desiccator. All surface analyses (EDX, EBSD, PL, ARPES) were performed on freshly cleaved surfaces.

3.1.3 Synthesis of $Cs_2BiAgBr_6$ single crystals

The synthesis was carried out according to the method described in the paper by Filip et al.[116] Crystallization was carried out from a solution containing 2 M CsBr, 1 M AgBr and 1 M $BiBr_3$. 4.256 g CsBr, 1.878 g AgBr and 4.487 g $BiBr_3$ were placed in a 10 ml measuring flask and weighed on analytical scales with 10^{-3} g accuracy. The powders were then poured over to the line with 48% HBr solution and stirred until dissolved. The resulting solution was filtered with a cellulose filter and placed in a 20 ml beaker. The sealed beaker was heated in a furnace to 150°C, incubated for 1 hour, then slowly cooled at a rate of 10°C per hour to room temperature. The resulting dark burgundy single crystals were removed from the reaction mixture and air dried until the solvent evaporated, then stored in a desiccator.

3.1.4 Synthesis of $MAPbI_3$ single crystals

The synthesis was carried out according to the method described in the paper by Abdelhady et al.[84] Crystallization was carried out from a solution containing 1.2 M MAI and 1 M PbI_2, an excess of MAI being necessary to avoid precipitation of lead iodide;

for this purpose, 1.344 g MABr and 3.670 g $PbBr_2$ were placed in a 10 ml measuring flask, weighed on analytical scales with 10^{-3} g accuracy. The powders were then poured over to the line with dimethylformamide and stirred to dissolving. The obtained solution was filtered with a cellulose filter and placed in a 20 ml beaker. The sealed beaker was heated in a water bath to 80°C and incubated for 4 hours. The resulting black single crystals were removed from the reaction mixture and air dried until the solvent evaporated, then stored in a desiccator.

3.1.5 Synthesis of bismuth-doped $CsPbBr_3$ powders

To obtain $CsPbBr_3$ powders, a solution with equimolar concentrations of bromide precursors with expected 2 g of the final product was used. To obtain Bi^{3+} doped powders, a portion of $PbBr_2$ was replaced by 0.1 M $BiBr_3$ solution in 48% HBr (Table 4), a given volume of which was placed using a micropipette at 2-20, 10-100 or 100-1000 µl in a beaker along with the bromide powders.

Table 4 Quantities of reagents for the synthesis of bismuth-doped $CsPbBr_3$ single crystals

Bi^{3+}/Pb^{2+} in solution	m_{CsBr} [g]	m_{CsBr} [g]	V_{BiBr_3} [ml]
0 %	0,734	4,406	0
0,025 %	0,734	4.404	0,009
0,05%	0,734	4,402	0,017
0,5 %	0,734	4,382	0,170
1 %	0,734	4,356	0,345
2 %	0,734	4,316	0,690
5 %	0,734	4,184	1,725

The obtained suspensions and $BiBr_3$ solution were placed in a glass beaker and poured into 50 ml of 48% HBr solution, and under constant stirring and heating to 80°C were brought to dissolution, after which also under constant stirring and heating to 120°C and gradually evaporated to obtain yellow to red-brown powders. To study low-temperature photoluminescence, the powders were mixed with Technovit epoxy resin and applied to the surface of monocrystalline silicon wafers, dried at 50°C in a desiccator, then polished to a flat mirror-like surface using diamond pastes of various diameters.

3.1.6 Synthesis of single crystals with heterojunction $MAPbBr_3/CsPbBr_3$

Since $CsPbBr_3$ is not soluble in precipitalion mixture $MAPbBr_3$, a pre-grown $CsPbBr_3$ crystal was put into the $MAPbBr_3$ growth solution to obtain a single crystal with a heterointerface as described above. The closed beaker was heated in a water bath to 80°C and incubated for 4 hours. The formed single crystals were removed from the reaction mixture and air dried until the solvent evaporated, after which they were placed in a desiccator for storage. All heterojunction studies were performed on freshly cleaved surfaces.

3.2 Research methods

3.2.1 Scanning Electron Microscopy

Scanning Electron Microscopy (SEM) is based on the interaction of an accelerated electron beam with a sample. During the interaction of the primary beam with the sample multiple acts of electron scattering and absorption occur in a drop-shaped area at the surface of the sample, the size of which is determined by the beam energy and the density of the sample material and can be as small as a few micrometres (Figure 3.1a) . The spatial resolution of the method depends on the magnetic optics, the primary beam energy and the properties of the sample under study and can reach fractions of a nanometre.

When accelerated electrons interact with matter, scattering and ionisation occur. The study of patterns of elastically reflected electrons from a flat sample - Electron Backscatter Diffraction (EBSD), provides information about the crystal structure of matter.

Additionally the scattered electron can escape from the sample surface after multiple impacts which cause a loss of energy and deflect it from its original direction. The intensity of back-scattered electrons thus carries information about the mass of the scattering atoms and therefore provide the phase contrast.

When a substance is ionised by an accelerated electron beam, secondary electrons are produced mainly from the conduction electrons of metals and the valence bands of semiconductors and dielectrics (Figure 3.1b). The energy of the secondary electrons is much lower than that of the backscattered electrons and the yield depth is therefore smaller, so the analysis of secondary electrons carries information about the surface topology.

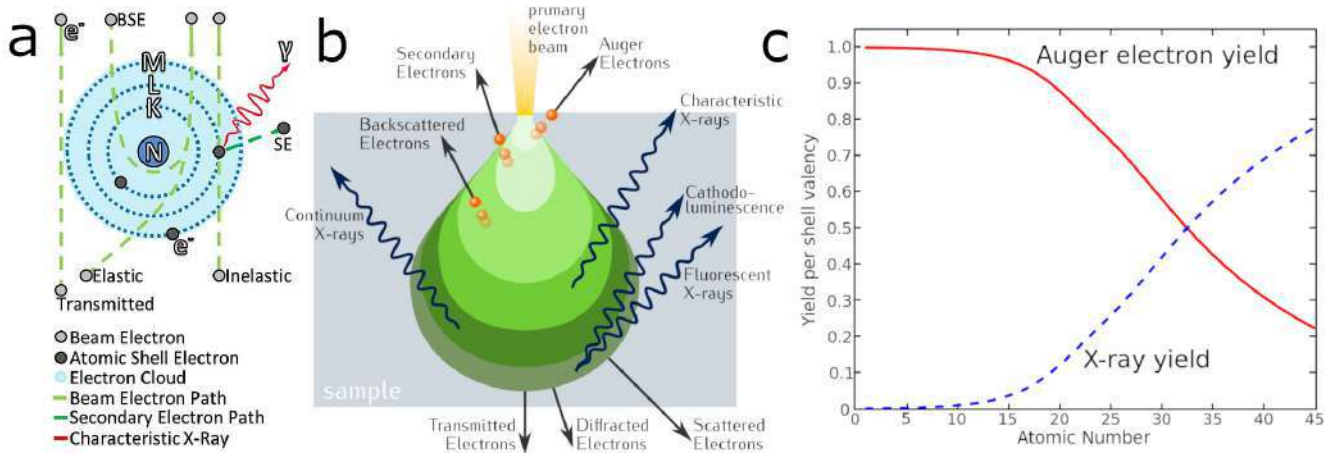

Figure 3.1 Electron beam interaction with matter[117]: (a) Types of interaction of electrons with matter, (b) model of electron beam interaction region with sample surface and (c) Auger and X-ray relaxation probabilities[117]

Ionization from inner shells entails relaxation in the form of Auger-electron emission for light atoms or characteristic X-ray emission for heavy atoms(Figure 3.1c). Since Auger-electrons have a very small yield depth (on the order of 1 nm), their detection only makes sense in ultra-high vacuum and is rarely used in electron microscopes in practice. The yield depth of X-rays is much greater and therefore their detection carries information on the elemental composition of the entire primary beam-sample interaction region (several μm^3) and is widely used for analysis.

There are two types of characteristic X-ray analysis in SEM: Energy-dispersive X-ray Spectroscopy (EDX) and Wavelength-dispersive X-ray Spectroscopy (WDS). EDX is a fast, wide wavelength range scanning using a photomultiplier tube (PMT), while WDS will decompose a narrow part of the spectrum on a diffraction grating to give clearly resolved lines. WDS analysis is used for precision quantitative measurements and spectral line superpositions.

The studies presented in this paper were carried out using a Hitachi S-3400N electron microscope with Oxford Instruments X-Max 20 for energy dispersion analysis, Inca Wave 500 System for wave dispersion analysis and AZtecHKL Channel 5 for back-scattered electron diffraction.

3.2.2 X-ray diffraction methods

X-ray diffraction methods are based on Rayleigh scattering of X-rays on atoms of matter. The secondary radiation has the same wavelength and phase, so the rays scattered

by atoms can interfere. Since the distances between atomic planes in crystals are comparable to the wavelengths of X-rays, crystals as materials with translational symmetry can serve as diffraction gratings, decomposing the primary beam.

X-ray diffraction analysis determines the atomic structure of a substance, which includes the size and shape of the spatial cell. Two basic methods of analysis are used: the Laue method is used for single crystals and the Debye-Scherrer method for polycrystals and powder samples.

By irradiating a fixed single crystal with an X-ray beam according to the Laue method, a diffraction pattern consisting of individual spots is obtained; its analysis makes it possible to determine the symmetry elements of the crystal and its orientation. Subsequent rotation around a chosen axis yields a diffraction pattern in which the spots are arranged in parallel layered lines formed by reflections from atomic planes. Analysis of this diffraction pattern makes it possible to precisely determine the coordinates of the atoms in the crystal.

In the case of Debye powder diffraction, an X-ray beam passing through a rotating polycrystalline sample forms a series of concentric circles on a perpendicular plane. From the resulting dependence of the radiation intensity on the scattering angle it is possible to determine the detailed arrangement of the atoms in the unit cell and the interplanar distances.

The studies presented in this work were carried out using a Xcalibur Eos single-crystal diffractometer, a Bruker D2 Phaser benchtop powder diffractometer, and a Bruker D8 Discover high resolution diffractometer.

3.2.3 Photoluminescence

When a semiconductor is excited by radiation whose wavelength exceeds its band gap, electrons from the valence band pass into the conduction band and thermalize at its bottom. During the reverse transition, in the case of a direct-gap semiconductor, there is spontaneous incoherent radiation equal in wavelength to the energy gap of the band gap. At low temperatures the main channel of radiative relaxation is exciton recombination. Moreover, the interaction of a free exciton with crystal defects, the so-called traps, is an advantageous process and in the case of recombination the photoluminescence spectra show an additional red shift of the emission bands. In the case of radiation-free recombination on traps, the photoluminescence intensity decreases.

The intensity of radiation caused by free exciton recombination has a superlinear dependence on the optical pumping power described in the two-particle approximation,

while in the case when the number of traps significantly exceeds the concentration of charge carriers, the intensity of exciton recombination radiation depends linearly on pumping and is described in the quasi-single-particle approximation.

Studying the intensity decay of the free exciton recombination line according to Arrhenius theory for processes with an activation energy makes it possible to know the lower limit for exciton binding energy.

Thus, in the low temperature region, when the photoluminescence lines are small and well resolvable, the spectra provide information about the type of band structure of the semiconductor, quantitative information about its quality, its band gap, exciton binding energy and radiative recombination at the traps.

The studies presented in this paper were carried out using Cryogenics CFM-7TS-H2-CFVTI-25-0 and Montana Cryostation helium cryostats at 405, 425 and 532 nm Continuous Wavelength lasers and a Horiba iHR550 spectrometer with a liquid nitrogen cooled CCD.

3.2.4 Raman spectroscopy

In terms of the classical theory, inelastic Raman scattering arises from the interaction of matter with excitation radiation: The monochromatic light induces electron polarisation and is scattered with an initial frequency ν_0 (Rayleigh scattering, the overwhelming part) and with frequencies $\nu_0 \pm \nu_1$, where ν_1 is the natural frequency of the vibrating matter. The wavelength of the excitation radiation is usually chosen in the transparency region of the sample in order to avoid photoluminescence, which has a much higher quantum yield.

The method is widely used for chemical analysis and more subtle effects of interactions between atoms of a substance.

The studies presented in this paper were performed using a Horiba T64000 research grade Raman spectrometer with a triple monochromator and a Peltier-cooled CCD and helium-cooled criocouple sample cell.

3.2.5 Photoelectron spectroscopy

Photoelectron spectroscopy is a surface method for the study of solids, based on the phenomenon of the photoelectron effect. Analysis of the energy distribution of photoelectrons knocked out from the surface of a solid by X-ray or UV-radiation provides information on the electronic states, vibrational and rotational levels. Because of the

high frequency of ionising radiation and the energy of the emitted electrons, the study of photoemission is one of the most sensitive and accurate techniques for measuring energies and shapes of electronic states and molecular and atomic orbitals as well as for detecting substances in trace amounts.

The research presented in this work was carried out using the Nanolab research platform equipped with a photoelectron spectroscopy analysis module.

3.2.6 Diffuse light reflection spectroscopy

Diffuse light reflection spectroscopy is a technique based on the collection and analysis of scattered visible and IR light. It is used to study fine particles and powders as well as rough surfaces, and requires minimal sample preparation.

When radiation strikes a sample, it may be reflected from the surface or transmitted by the substance. After numerous acts of reflection-permission, the radiation is collected by a spherical mirror and focused on the detector, the analysis of the radiation carries information about the absorption of the sample.

The studies presented in this paper were performed using a Perkin Elmer LAMBDA 650 UV/Vis spectrophotometer.

Chapter 4. Experimental results and discussion

4.1 Confirmation of the composition and structure of synthesized halide perovskites single crystals

The results presented in section 4.1, section 4.2 and section 4.3 are published[16;118].

In the course of the study, the synthesis of one of the most popular at the moment halide perovskite materials of the general formula ABX_3 - methylammonium tribromoplyumbate $MAPbBr_3$, as well as products of ion substitution in its composition were synthesized.

The tolerance factor of $MAPbBr_3$ is τ=0.93, close to 1, which explains its high stability and ease of synthesis. The substance transition to a high-temperature, highly symmetric cubic phase takes place at 230 K[119].

Replacement of cation A with smaller cesium to form $CsPbBr_3$ leads to distortion of the structure, the tolerance factor drops to τ=0.85 and at room temperature the substance exists in an orthorhombic phase, and the transition to cubic through tetragonal is observed only at 370 K[119].

The influence of lead cation replacement in position B was studied in its replacement with heterovalent pair $Ag^{+}Bi^{3+}$ to form compound $Cs_2BiAgBr_6$, which has cubic crystal lattice at room temperature, calculated tolerance factors for silver and bismuth cations respectively τ_{Ag}=0.84 and τ_{Bi}=0.89. According to the data of single crystal X-ray diffraction analysis, the obtained single crystals have the structure of elpasolite $Fm-3m$ with lattice constant a = 11.197(1) Å.

The replacement of the X anion by a larger iodine ion with the formation of $MAPbI_3$ also leads to distortions of the crystal symmetry, the structure tolerance factor is τ=0.91, and the transition to the cubic phase is observed only at 330 K[26]. The microphotographs of the synthesized single crystals are shown in Figure 4.1.

The structure and composition of the obtained single crystals were confirmed by backscattered electron diffraction and energy dispersion analysis (Figure 4.2).

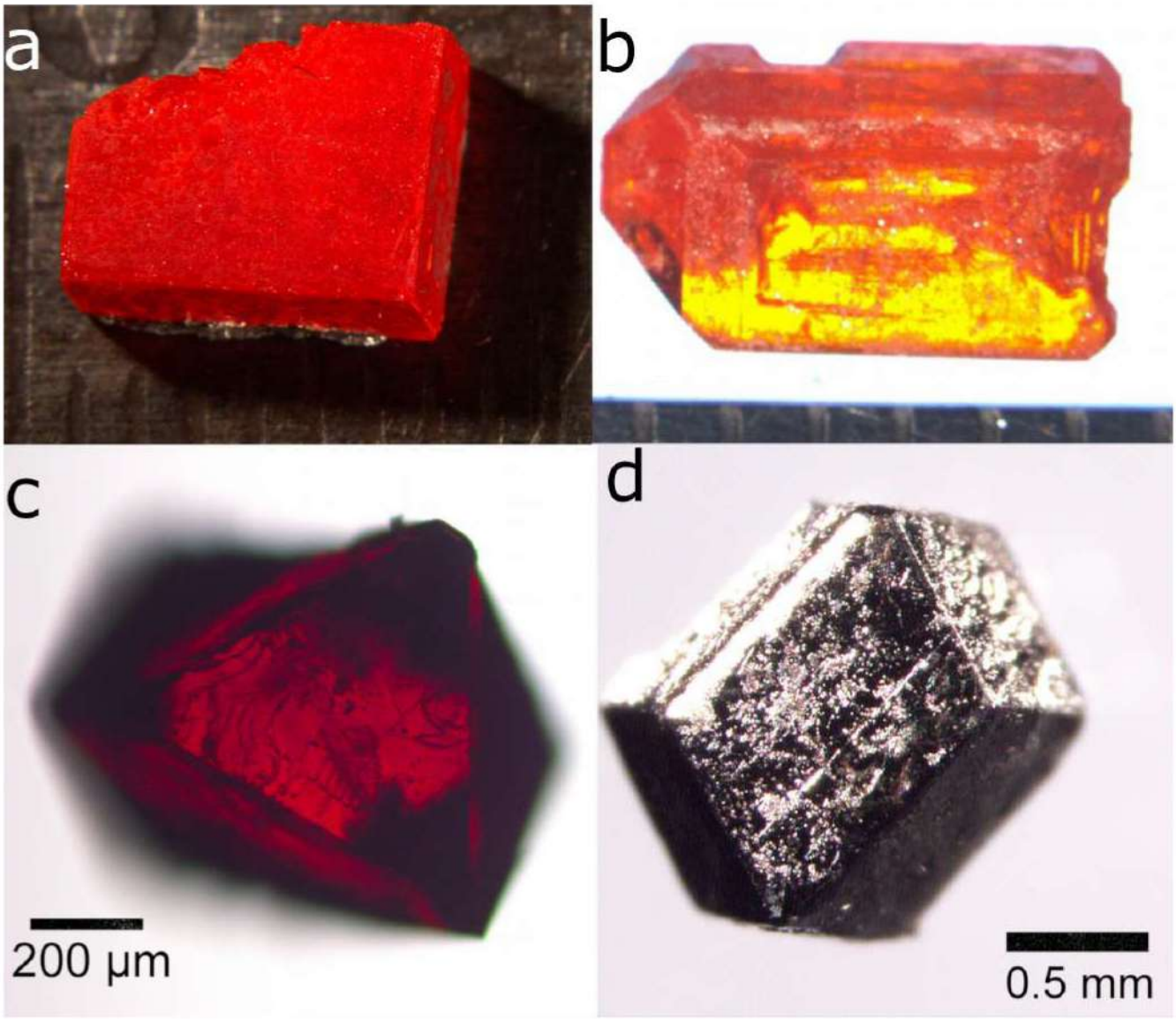

Figure 4.1 Microphotographs of (a)$MAPbBr_3$, (b) $CsPbBr_3$, (c) $Cs_2AgBiBr_6$ and (d) $MAPbI_3$ single crystals

4.2 Low-temperature photoluminescence of $MAPbBr_3$, $CsPbBr_3$, $Cs_2AgBiBr_6$ and $MAPbI_3$ single crystals

Low-temperature photoluminescence spectra were recorded for all synthesized single crystals with 532 or 425 nm continuous laser irradiation excitation, depending on the band gap width of the material under study.

At room temperature, $MAPbBr_3$ and $CsPbBr_3$ single crystals have very similar bright orange coloration due to high self absorption of luminescence[120], but on cooling the color of $CsPbBr_3$ changes to a transparent light yellow, whereas the color of $MAPbBr_3$ is almost unchanged. Self-absorption is caused by the formation of indirect Rushba transition, typical for crystals with inverse symmetry caused by the

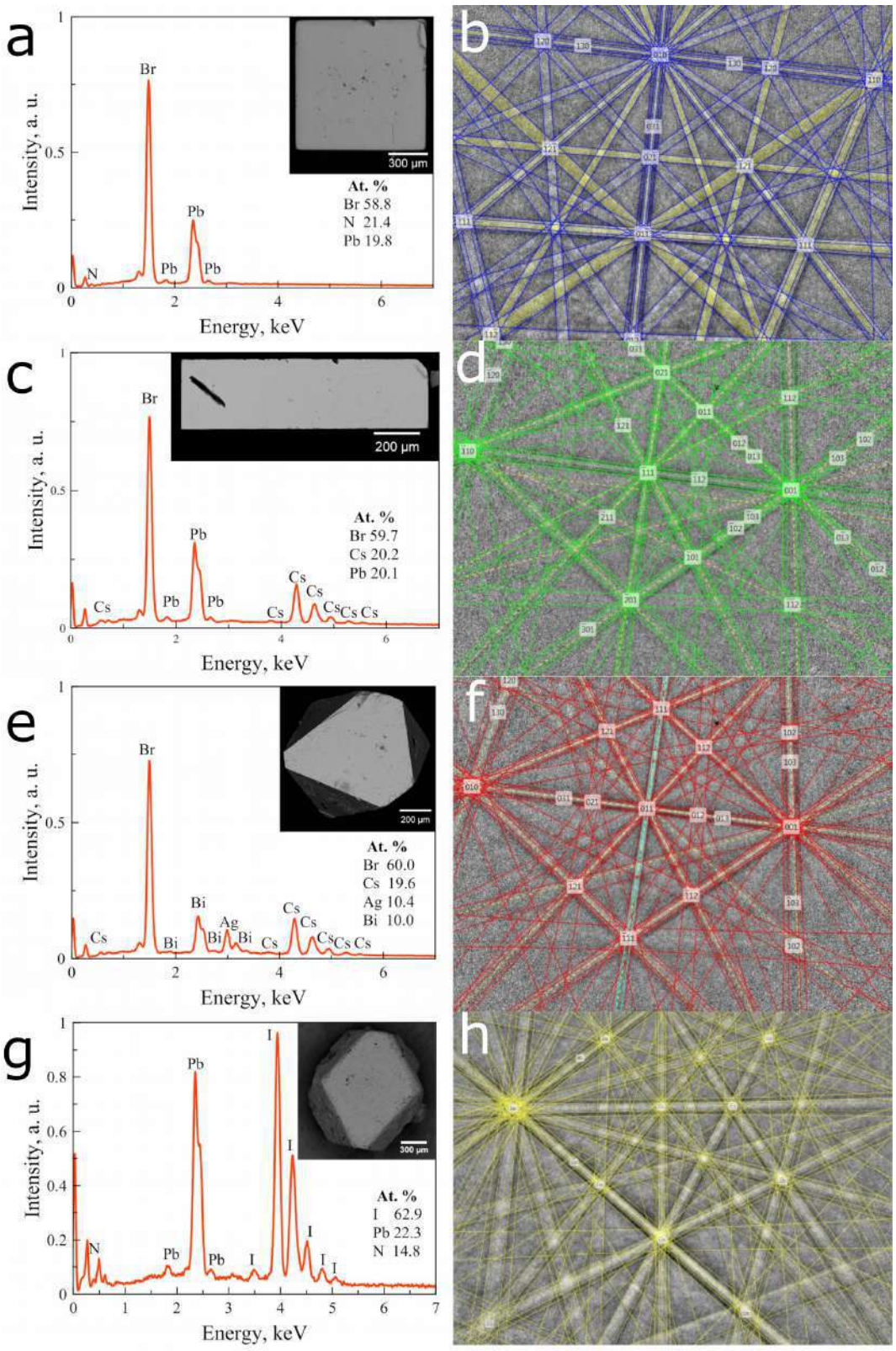

Figure 4.2 Energy-dispersive spectra and backscattered electron diffraction lines for (a, b)$MAPbBr_3$, (c, d) $CsPbBr_3$, (e, f) $Cs_2AgBiBr_6$ and (g, h) $MAPbI_3$

non-spherical shape of MA^+ cation and random thermal fluctuations of cesium cations at high temperatures. However, because of the high mass of the cesium cation at

low temperatures, degeneracy occurs and self absorption disappears, causing the color change[121].

$MAPbBr_3$, $CsPbBr_3$, and $MAPbI_3$ show a similar spectral structure: an intense narrow line and broader and less intense bands shifted to the red region (Figure 4.3). We attribute the narrow peak to the recombination of the free exciton[122] due to the super-linear dependence of its intensity on the optical pumping. The main photoluminescence line of $CsPbBr_3$ (2.32 eV at 3 K) exhibits a slight blue shift relative to $MAPbBr_3$ (2.25 eV at 1.4 K) due to the smaller Cs^+ radius compared to MA^+ and elongated Pb-Br bonds, while $MAPbI_3$ (1.64 eV at 3 K) shows a significant red shift. The intensity of the band shifted to the red region depends linearly on the pumping and, as the temperature increases, it departs from the free exciton peak for each crystal by constant values, which makes it the peak of radiative exciton recombination at the trap. Consistent with literature data, for $MAPbBr_3$ this trap (25 meV) may be due to excess MABr in the reaction medium during single crystal deposition[123]. The main defects in the crystal structure of $CsPbBr_3$ and $MAPbI_3$ having low formation energies form close levels in the band gap, which makes it difficult to determine whether the peaks (25, 30 and 40 meV for $CsPbBr_3$ and 5, 15 and 18 meV for $MAPbI_3$) belong to defects[76;78].

As the temperature increases, the exciton recombination line experiences a blue shift and broadening (Figure 4.4). The observed blue shift, in general, is unusual for semiconductors, whose bandgap width usually decreases with the heat-induced increase in the interatomic distance[124]. In the case of perovskites, however, thermal expansion of the crystal lattice reduces the overlap between the Pb $6s$ and X np antibonding orbitals that form the VBM, causing the bandgap increase[34].

Extrapolation of the linear dependence of the line half-width at half-height to 0 K gives non-radiation decay rates around Γ_{NR}=0.5 meV for $MAPbBr_3$ and $CsPbBr_3$, and Γ_{NR}=1.4 meV for $MAPbI_3$, which appears to be related to the lower quality of the crystal studied. For the best gallium arsenide-based heterostructures grown by molecular beam epitaxy, this value is 0.137 meV[125], indicating the high optical quality of the examined crystals.

Approximating the change in the exciton recombination intensity with increasing temperature by the Arrhenius formula $I = \frac{I_0}{1+Ae^{\frac{E_b}{kT}}}$, for the exciton binding energy, we obtain lower estimates of E_b=13 meV for $MAPbBr_3$, 17 meV for $CsPbBr_3$, and 5.5 meV for $MAPbI_3$ (Figure 4.4), which agree well with the literature data[76;122] and with the dependence of exciton binding energy on bandgap width observed in semiconductors (Figure 4.5): exciton binding energy is inversely proportional to the background dielec-

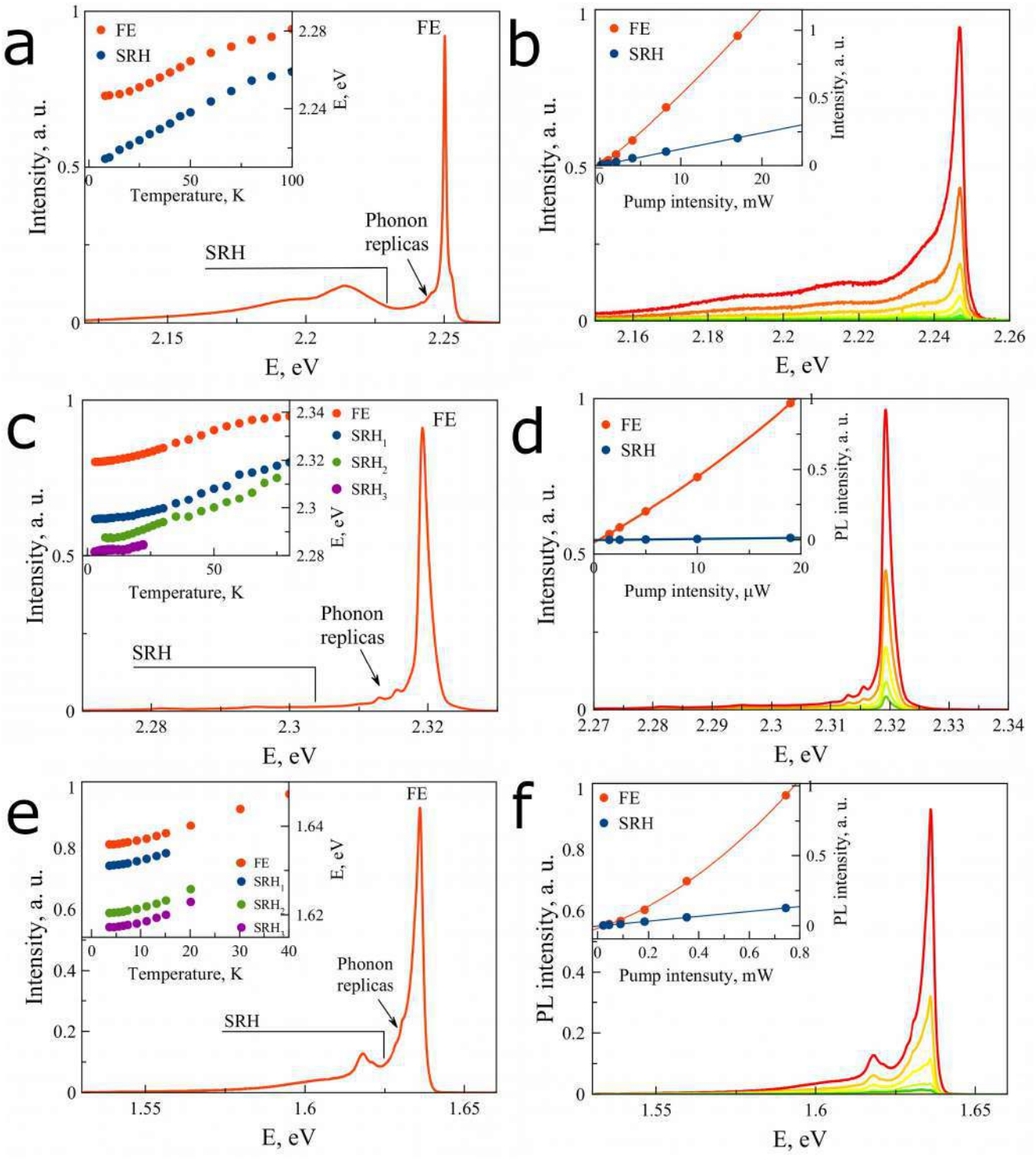

Figure 4.3 Low-temperature photoluminescence of halide perovskite single crystals: photoluminescence spectra of (a, b) $MAPbBr_3$ at 1.4 K, (c, d) $CsPbBr_3$ at 3 K and (e, f) $MAPbI_3$ at 3 K, demonstrating free exciton (FE), radiative recombination on defects (SRH) and phonon replicas.Insets demonstrate the FE and SRH peaks intensities dependencies on the temperature.

tric constant, which describes screening of Coulomb interaction in the crystal, which depends on virtual interband transitions. These transitions become less and less proba-

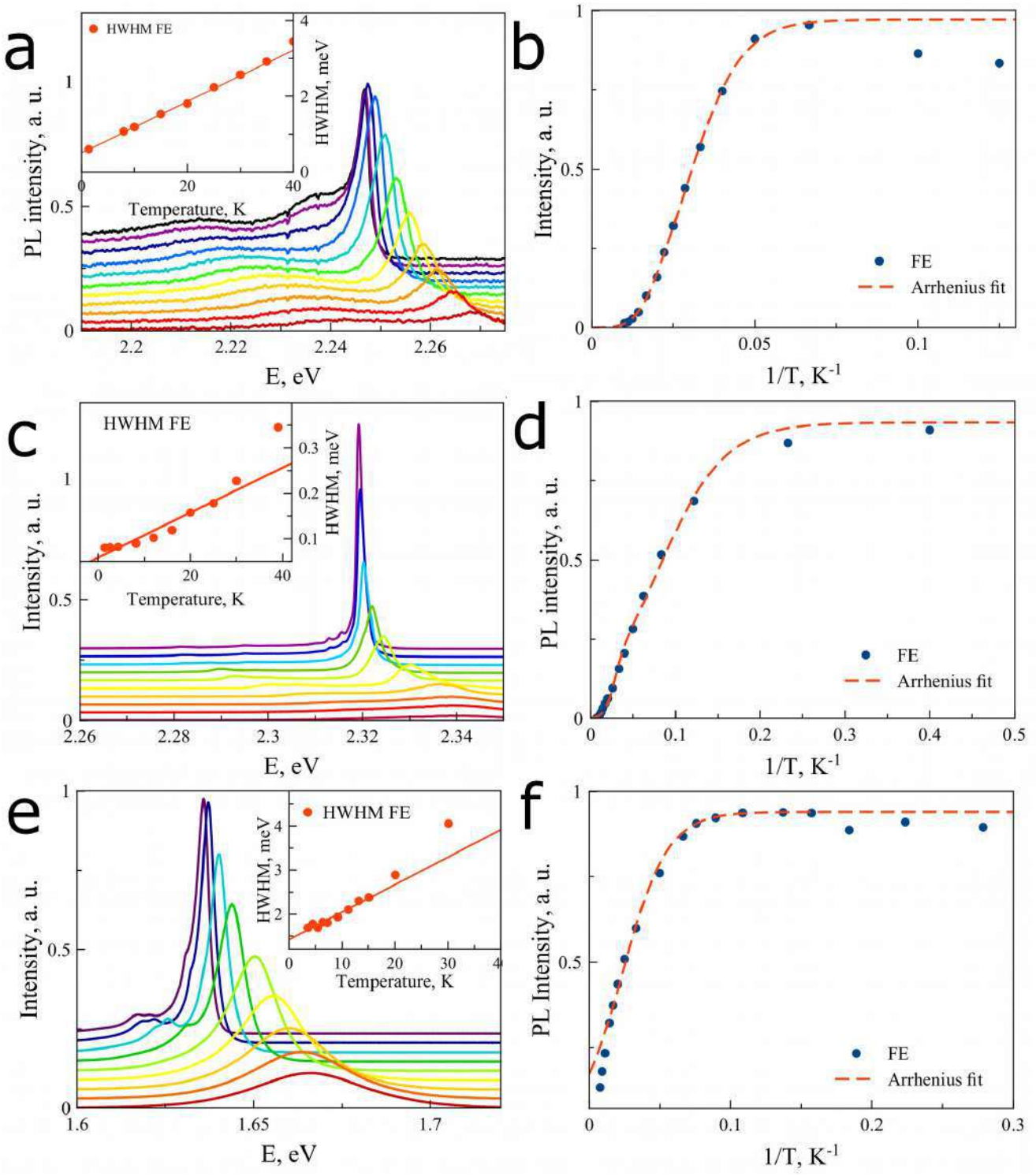

Figure 4.4 Shift of photoluminescence peak positions of halide perovskite single crystals with temperature changes (insets demonstrate half-width at half maximum dependence of free exciton peak on material temperature) and photoluminescence intensity dependence on temperature fit by Arrhenius equation for (a, b) $MAPbBr_3$, (c, d) $CsPbBr_3$ and (e, f) $MAPbI_3$.

ble as the bandgap width increases, and as a result the exciton coupling energy increases for wide-gap materials[126]. Unlike the other substances presented, according to theo-

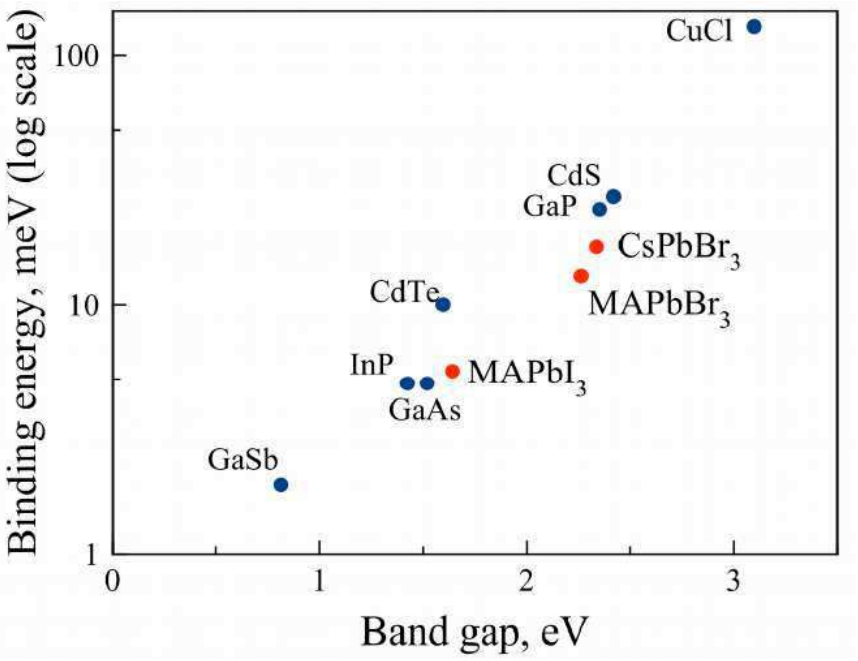

Figure 4.5 Exciton binding energies vs. bandgaps for some traditional semiconductors (blue dots) and investigated lead-based halide perovskites (red dots)

retical modeling[116], $Cs_2AgBiBr_6$ is an indirect-gap semiconductor with lowest indirect transitions of 1.83 eV (L-X) and 1.97 eV (G-X) and direct 2.51 eV (X) (Figure 4.6a).

The low-temperature photoluminescence intensity of $Cs_2AgBiBr_6$ is about two orders of magnitude lower than that of its lead analogue $CsPbBr_3$ obtained under the same conditions (Figure 4.6b). This correlates well with the indirect-gap nature of the material, since interband recombination of indirect-gap semiconductors involving phonons has a low probability, especially at low temperatures. The most intense photoluminescence peak has an energy of 1.946 eV and corresponds to the first indirect L-X transition. Less intense peaks at 2.095 eV and 2.254 eV refer, respectively, to the second indirect G-X and the first direct X-X transitions. The half-width at half-height of the peaks at 1.946 eV and 2.095 eV is about 70 meV, and the peak at 2.254 eV about 150 meV. Such large values at low temperatures when thermal homogeneous broadening is negligible imply significant inhomogeneous broadening, which also agrees well with the indirect-gap character of the material and the flat shape of the band structure maxima obtained by theoretical simulations.

4.3 Raman spectroscopy and phonon replicas of halide perovskites single crystals

In the low-temperature photoluminescence spectra of $MAPbBr_3$, $CsPbBr_3$, and $MAPbI_3$ single crystals a number of low-intensity but resolved peaks shifted relative to the free

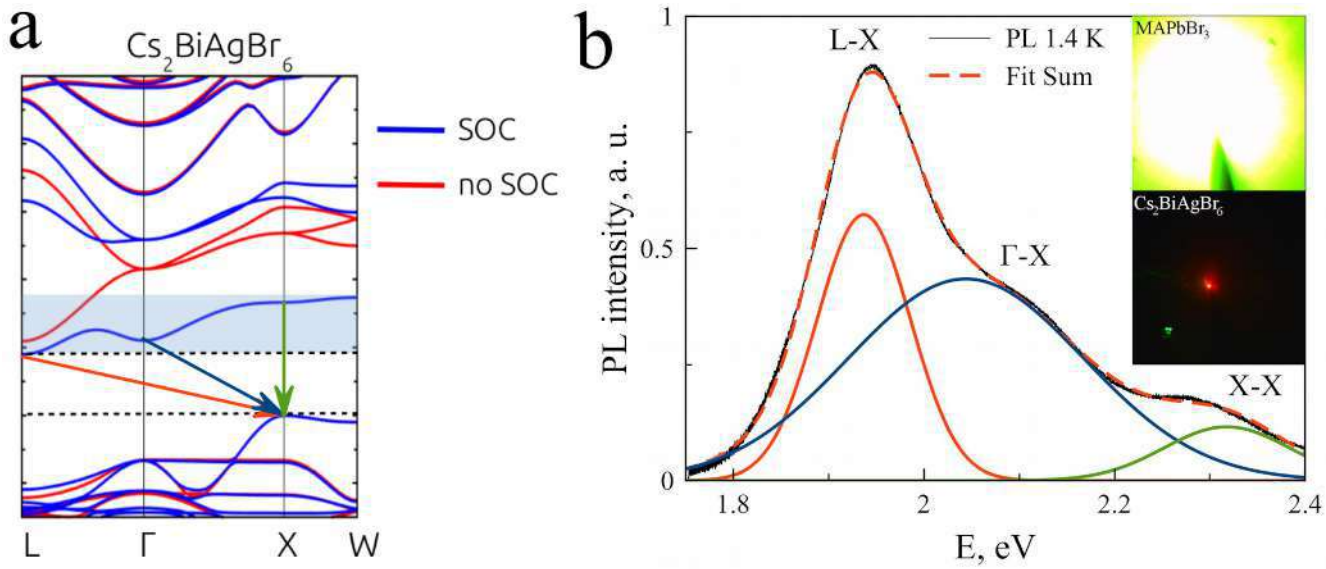

Figure 4.6 (a) Theoretical simulation of the band structure of $Cs_2AgBiBr_6$ with (blue lines) and without the spin-orbit interaction (red lines)[116], the arrows indicate the lowest electronic transitions: L-X (red), G-X (blue), and X-X (green), (b) the low-temperature photoluminescence spectrum of $Cs_2AgBiBr_6$, decomposed into three Gaussians corresponding to the lowest electronic transitions and microphotographs of PL $MAPbBr_3$ and $Cs_2AgBiBr_6$ in inset

exciton peak by several meV into the red region were observed. A complementary study of Raman scattering at low temperatures in the low-frequency region was carried out to investigate from the nature. The samples were excited in the region of material transparency by laser pumping with a continuous laser with a wavelength of 770 or 830 nm.

According to the theoretical simulations for $MAPbI_3$[127] and $CsPbBr_3$[128;129] obtained Raman scattering lines were compared with the crystal lattice vibrations of the material (Figure 4.7a). Since the structure of $CsPbBr_3$ is close to $MAPbBr_3$, the modes associated with [$PbBr_6$] octahedra vibrations having the maximum intensity in the low-frequency region are close in energy for both materials.

The position of the free exciton peak satellites is in strict agreement with the position of the Raman scattering lines (Figure 4.7b), which allows the photoluminescence lines to be matched to phonon replicas with frequencies of 38, 48 and 67 cm^{-1} for $MAPbBr_3$, 33, 51 and 75 cm^{-1} for $CsPbBr_3$ and 46 and 57 cm^{-1} for $MAPbI_3$.

In conclusion, the high optical quality of the studied halide perovskite single crystals with small broadening of the low-temperature photoluminescence lines allows the observation of low-frequency phonon replicas in the spectra confirmed by Raman scattering. In the case of $Cs_2AgBiBr_6$ photoluminescence has two orders of magnitude

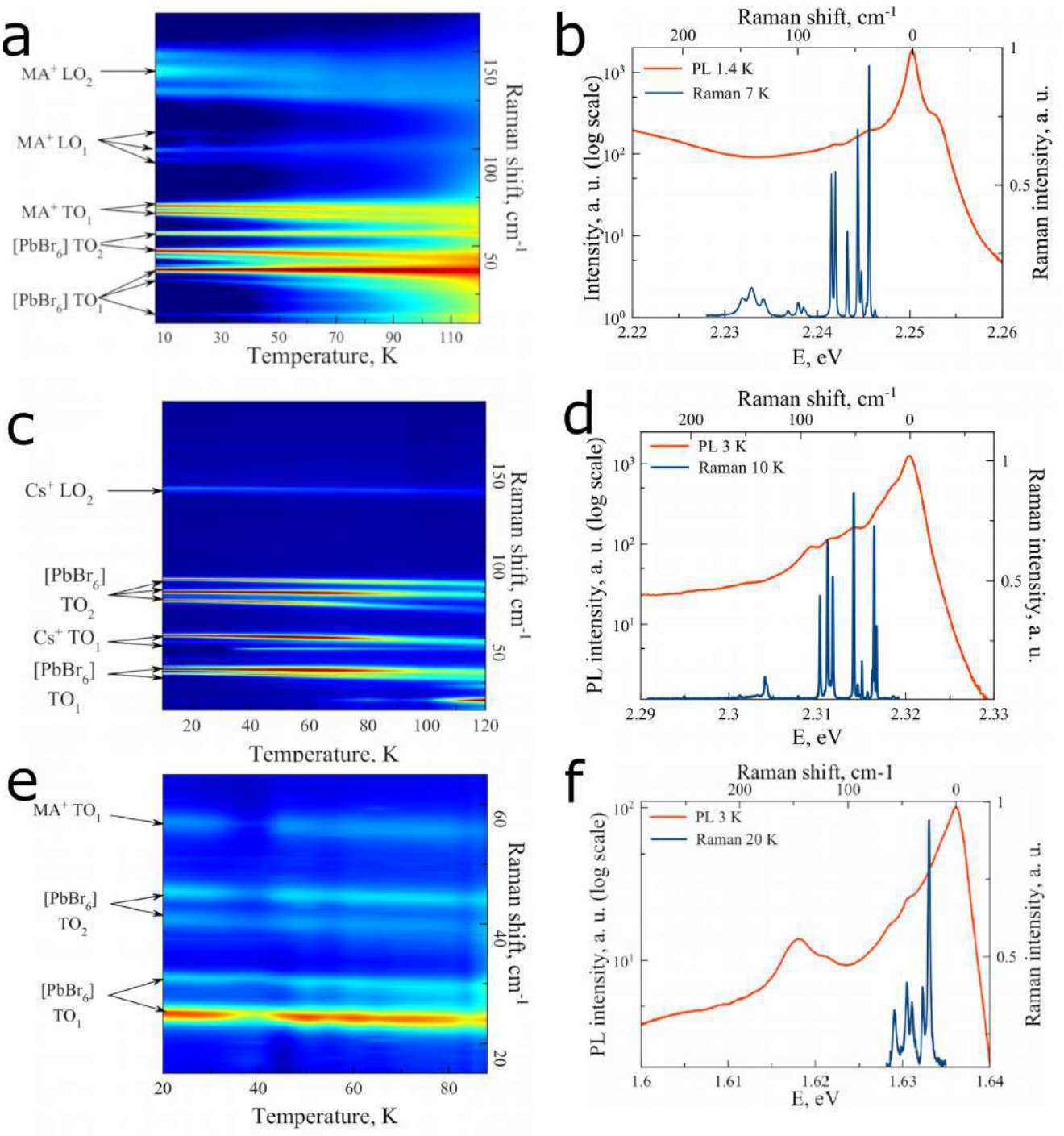

Figure 4.7 Temperature dependences of Raman scattering and correlation of phonon replicas with lines low-temperature Raman scattering for (a, b) $MAPbBr_3$, (c, d) $CsPbBr_3$ and (e, f) $MAPbI_3$.

lower quantum yield due to the indirect-gap nature of the material, the lines of the low-temperature photoluminescence spectrum were correlated with the lowest indirect electronic transitions.

4.4 Investigation of optical properties with electronic doping

The results presented in section 4.4 are published[130;131].

A number of bismuth-doped $CsPbBr_3$ single crystals and powders were synthesized to study electronic doping on the optical properties of halide perovskites.

The synthesis of single crystals was carried out by crystallization in the presence of precipitant. The addition of bismuth significantly changes the crystals colouration (Figure 4.8).

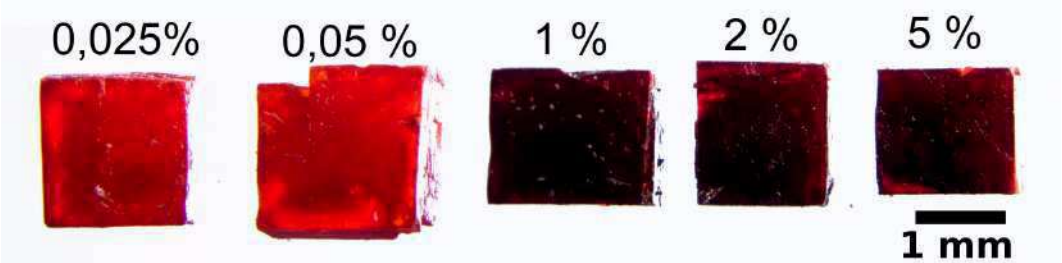

Figure 4.8 Photographs of $CsPbBr_3$ single crystals with different bismuth doping concentrations

The correspondence of the composition and structure of the single crystals to the $CsPbBr_3$ compound was confirmed by the methods of back-scattered electron diffraction and energy dispersive X-ray analysis (Figure 4.9).

The study of cleaved crystals by scanning electron microscopy in the back-scattered electrons contrast did not reveal side phases. Bismuth is reluctant to be embedded in the crystal lattice, its concentrations are outside the limits of determination by energy dispersive analysis. X-ray photoelectron spectroscopy analysis was

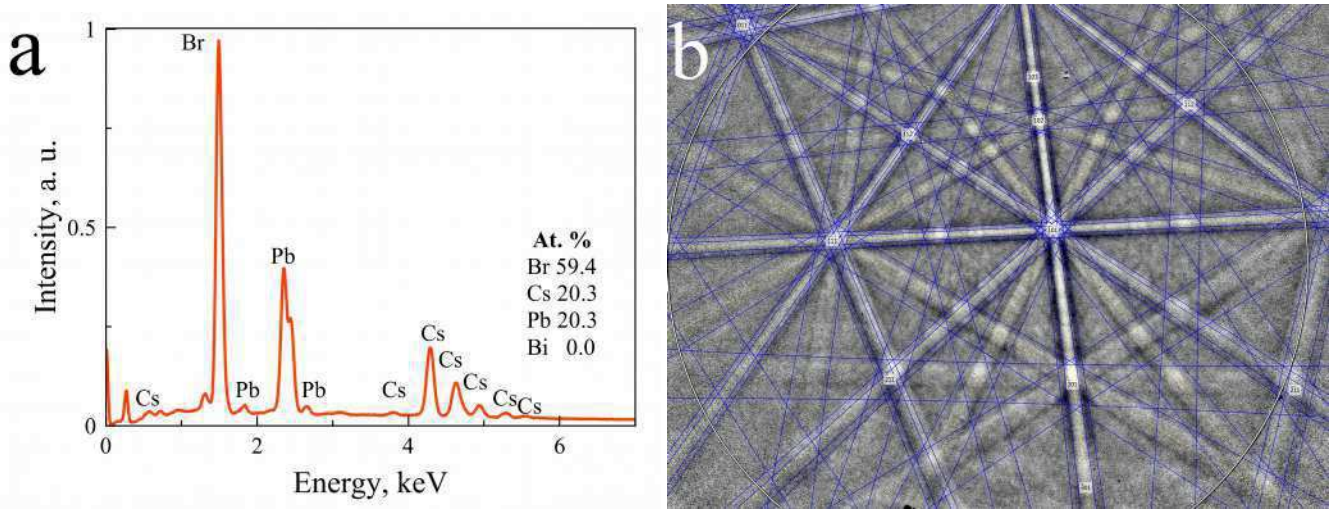

Figure 4.9 (a) EDX spectrum of $CsPbBr_3$ 5% Bi/Pb monocrystal, (b) EBSD pattern with Pnma solution of $CsPbBr_3$ 5% Bi/Pb monocrystal

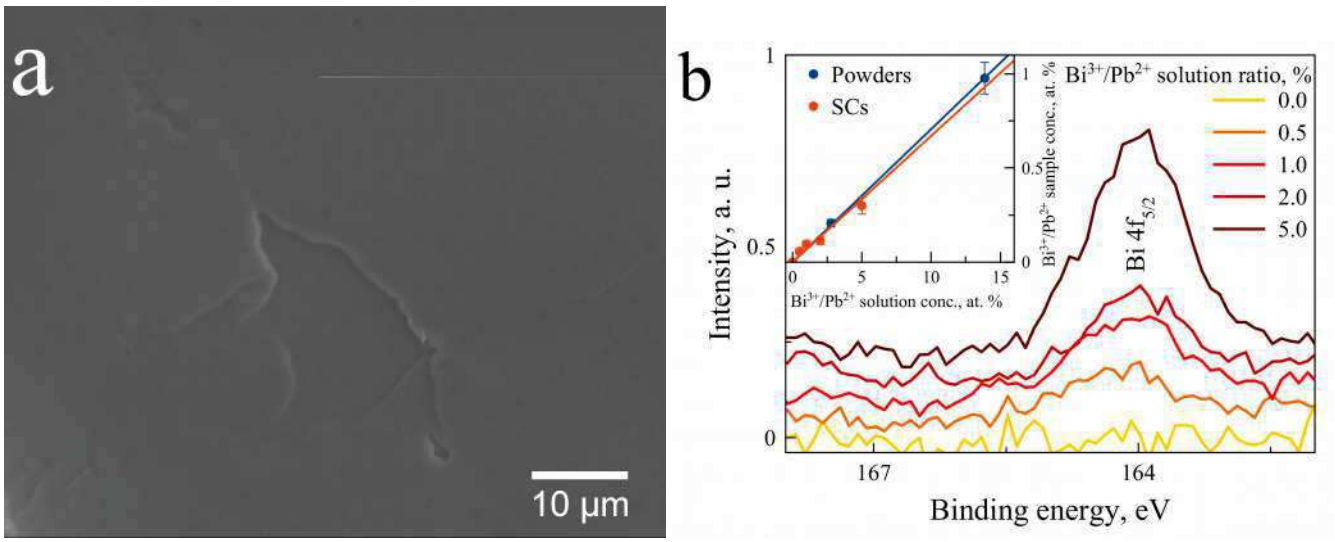

Figure 4.10 (a) SEM image of the surface of the $CsPbBr_3$ 5% Bi/Pb single crystal cut, no inclusions of other phases are observable on the surface, (b) XPS peak of Bi in doped single crystals. Bi content in powders (by ICP-MS) and single crystals on the tab

performed to determine the concentration of bismuth, and a linear dependence of the intensity of the strongest Bi $4f_{7/2}$ peak on the concentration of bismuth salt in solution during synthesis was plotted. The concentration of bismuth in the crystal with the highest doping concentration was determined from the M_{beta} line by wave dispersive X-ray analysis and was 0.3 at. %, which is in agreement with the literature data for the doping of $MAPbBr_3$[84;90;91](Figure 4.10).

The powders were synthesized from acidic aqueous solutions by evaporation. X-ray diffraction analysis and scanning electron microscopy and energy dispersive X-ray analysis revealed no side phases (Figure 4.11); the bismuth concentration in the powders was determined by inductively coupled plasma excitation atomic emission spectroscopy (Shimadzu ICPE-9000 optical emission spectrometer) and corresponds to the content in the single crystals (Figure 4.10b).

The diffuse reflectance spectra of doped perovskite powders show similar behavior to the results observed in the paper by Abdelhady et al.[84] - a significant shift (up to 170 meV with saturation) of the Urbach tails into the red region (Figure 4.12).

However, the position of the free exciton line in the low-temperature photoluminescence spectra of single crystals when excited by a 425 nm continuous laser (3.6 K) experiences only a slight shift to the red region due to inelastic scattering of excitons on defects of the crystal structure (Figure 4.13a). At these temperatures, the half-width of

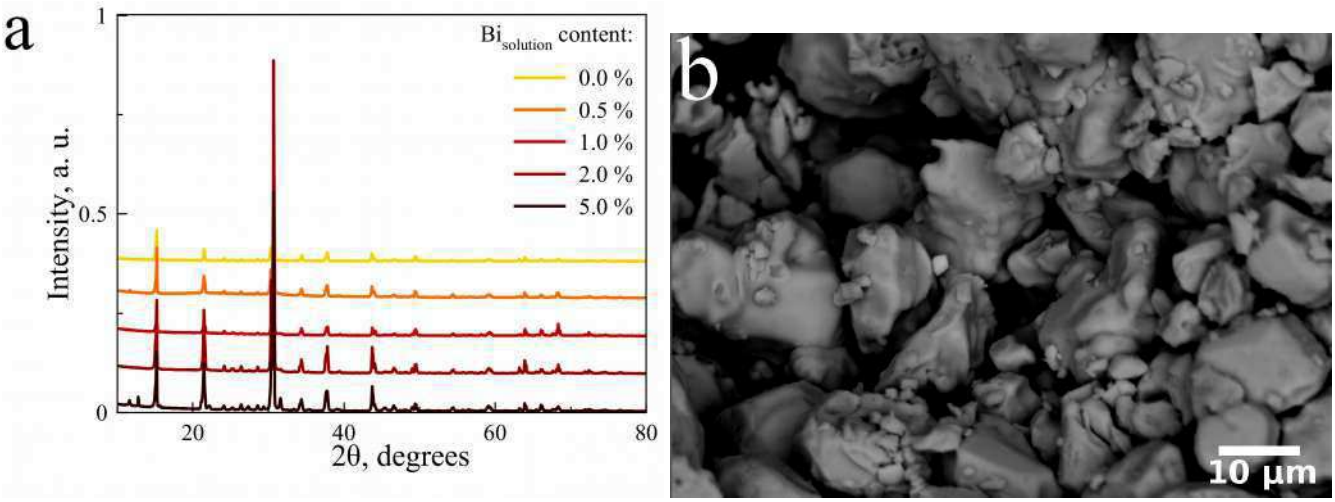

Figure 4.11 (a) X-ray diffractograms of bismuth-doped $CsPbBr_3$ powders, (b) SEM image of $CsPbBr_3$ powder 5% Bi/Pb

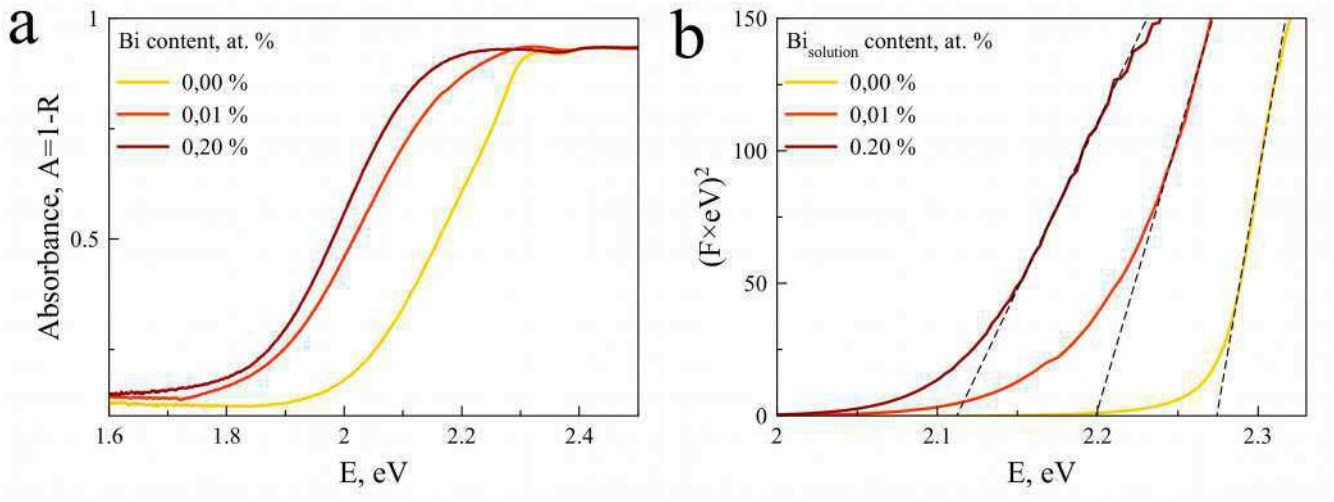

Figure 4.12 (a) Diffuse light reflection spectra of bismuth-doped $CsPbBr_3$ powders, (b) Tauc plots for calculating the optical gap

the PL peak is close to the value of the non-radiative relaxation rate, which characterizes the quality of the crystal. The HWHM value consistently increases with the addition of bismuth, which agrees well with the increasing values of microvoltages calculated in [91], and the photoluminescence intensity significantly decreases, which in this case is explained primarily by the non-radiation recombination at the traps.

In order to study more thoroughly the influence of bismuth on the formation of defects in the material, the low-temperature PL of Bi-added $CsPbBr_3$ powders synthesized in an excess of hydrogen bromide was investigated. According to theoretical simulations[76], the main defects in the band gap of $CsPbBr_3$ with low formation energy are V_{Cs}, V_{Pb}, V_{Br} and antistructure defect Pb_{Cs} . The large excess of HBr in the syn-

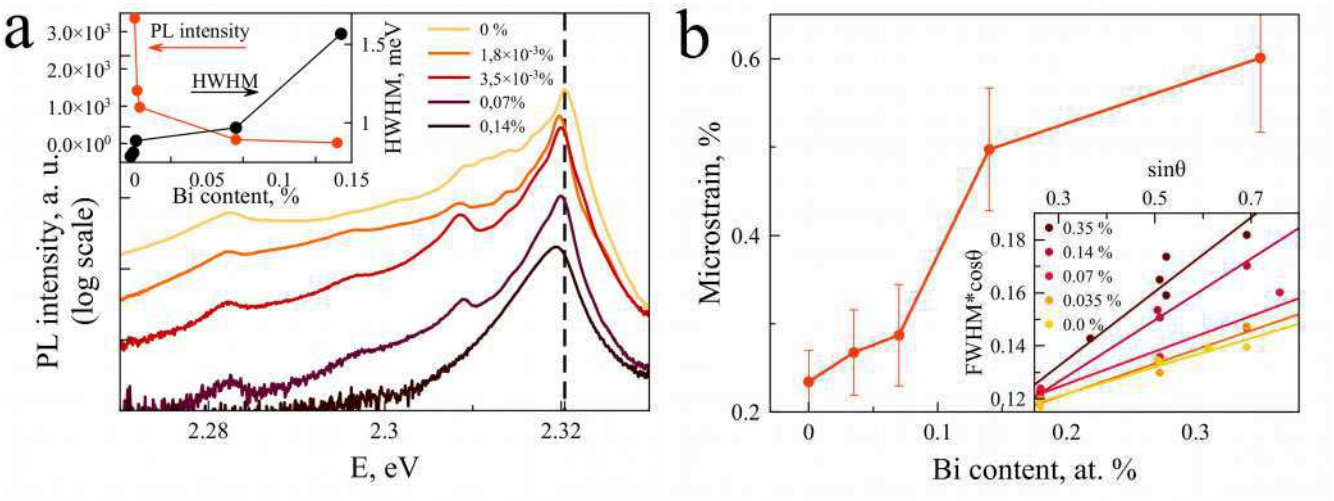

Figure 4.13 (a) PL spectra of bismuth-doped $CsPbBr_3$ single crystals, intensity values and HWHM of free exciton from bismuth concentration (on the tab), (b) microstress values of $CsPbBr_3$ crystals doped with bismuth, calculated from XRD data (Williamson-Hall plots on the inset)

thesis suggests a significant reduction in the probability of anion vacancy formation. In the low-temperature spectrum of underdoped $CsPbBr_3$ powder, the free exciton peak, broadened relative to the monocrystal, shifted into the red region due to inelastic scattering of excitons on defects in the crystal structure, and the recombination peak on a shallow defect, shifted by 25 meV into the red region, corresponding to the position of the cation vacancy as calculated, are well resolved. When bismuth was introduced, the photoluminescence of the powder shows only the cation vacancy peak and the photoluminescence intensity decreases drastically(Figure 4.14).

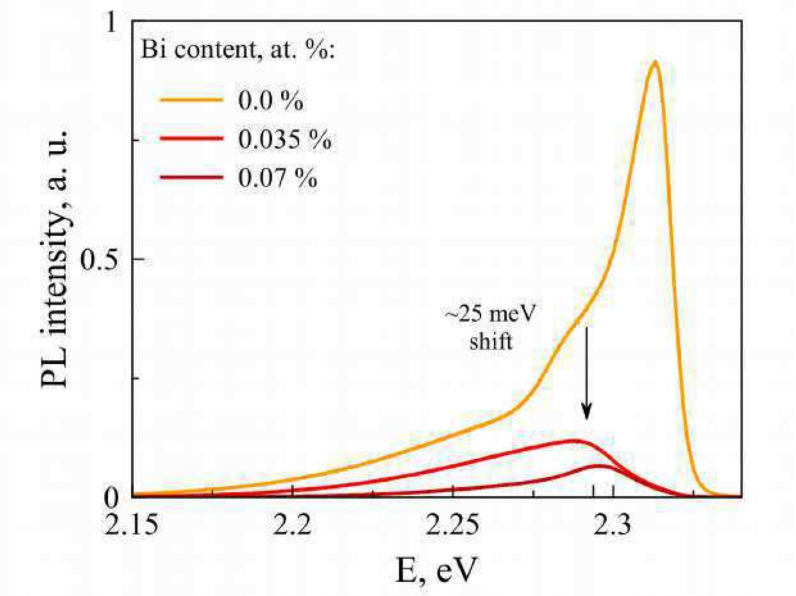

Figure 4.14 Photoluminescence spectra of bismuth-doped $CsPbBr_3$ powders

This result may indicate that the introduction of a heterovalent Bi^{3+} impurity with an excess positive charge stabilizes the formation of a negative cation vacancy[84] . The observation of a shift in optical absorption of thin films in the work by Yamada[90] when bismuth is embedded at 30 meV in the red region may also be due to an increase in the concentration of the fine trapped cation vacancy. The detuning of the recombination peak on defects in the photoluminescence spectra of $MAPbBr_3$ from the free exciton peak remains constant as the temperature increases[16].

According to photoelectron spectroscopy (UPS), the structure of the valence band does not change with bismuth doping (Figure 4.15). Electron doping causes a 0.6 eV rise in the Fermi level. In the paper by Zhang et al.[87] the invariability of the VBM position with the change of the crystal coloration during bismuth doping of $MAPbCl_3$ was shown.

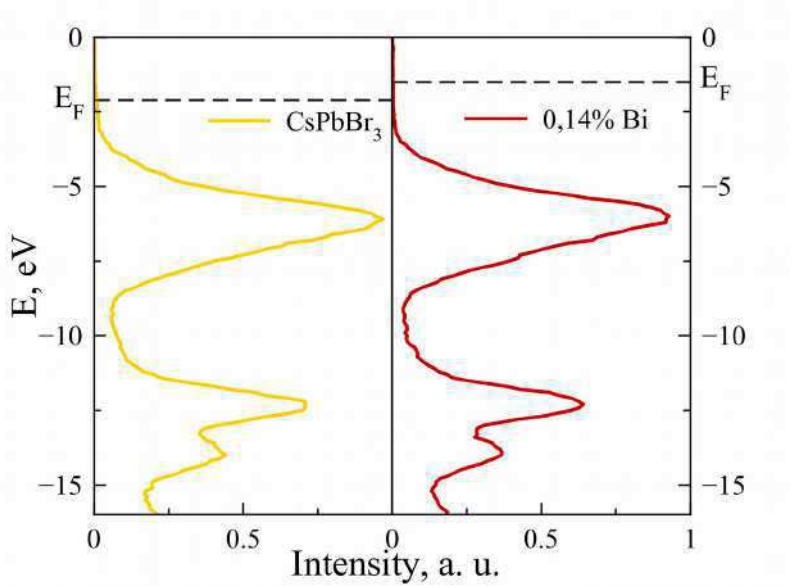

Figure 4.15 Structure of the valence band of bismuth-doped $CsPbBr_3$ single crystals according to UPS data

Thus, the observed significant shift of absorption into the red region caused by bismuth doping is caused by the disturbance of the crystal order of the materials and the shift of Urbach tails and is not associated with a change in the bandgap width. The effect of bismuth doping on the optical properties of halide perovskites is expressed in the broadening and weak red shift of the free exciton line due to increasing microstresses and a sharp decrease in the PL intensity due to radiation-free recombination on the traps.

4.5 Optical properties of halide perovskites heterostructure

To study the principle possibility of formation of an abrupt heterojunction between two perovskites, a sample with a $MAPbBr_3/CsPbBr_3$ heterointerface was synthesized. Since the solution for the synthesis of $MAPbBr_3$ does not etch $CsPbBr_3$, a simple growth of the $MAPbBr_3$ layer on a single-crystal $CsPbBr_3$ seed was performed. An optical micrograph of the chipped sample is shown in Figure 4.16.

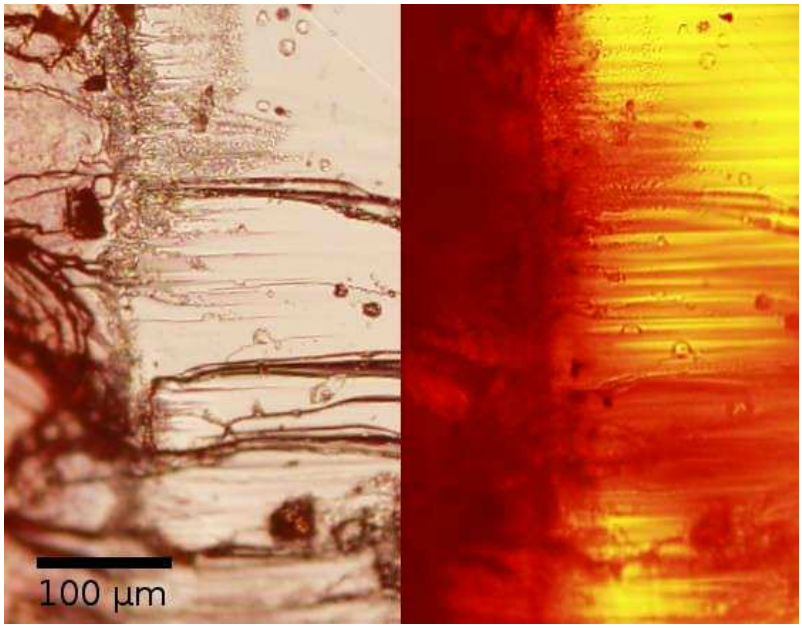

Figure 4.16 Optical micrographs of cleaved single crystal surface near $MAPbBr_3/CsPbBr_3$ heterojunction in reflected and transmitted light mode

The composition of the phases was confirmed by EDX Figure 4.17, with element distribution maps near the heterogeneous boundary demonstrating the absence of a transient gradient layer.

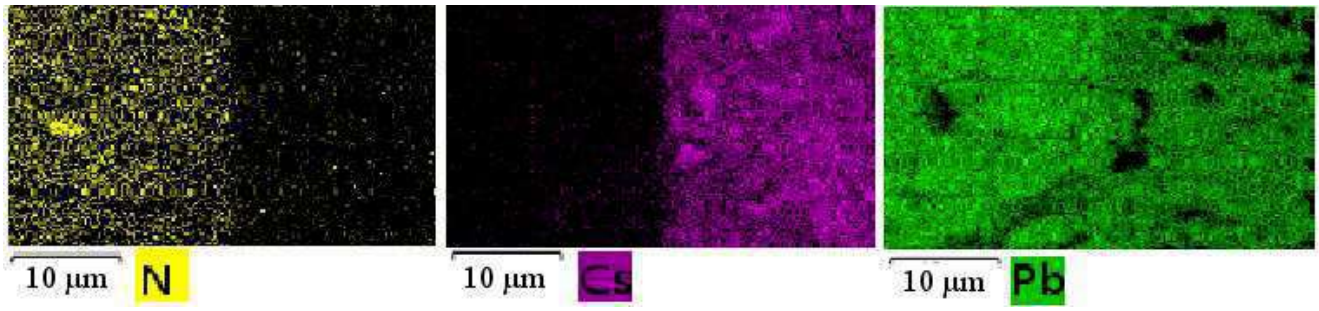

Figure 4.17 EDX maps of element distribution near the $MAPbBr_3/CsPbBr_3$ heterointerface

Scanning electron microscope images in backscattered electron contrast show an abrupt transition between two phases of different densities. Backscattered electron

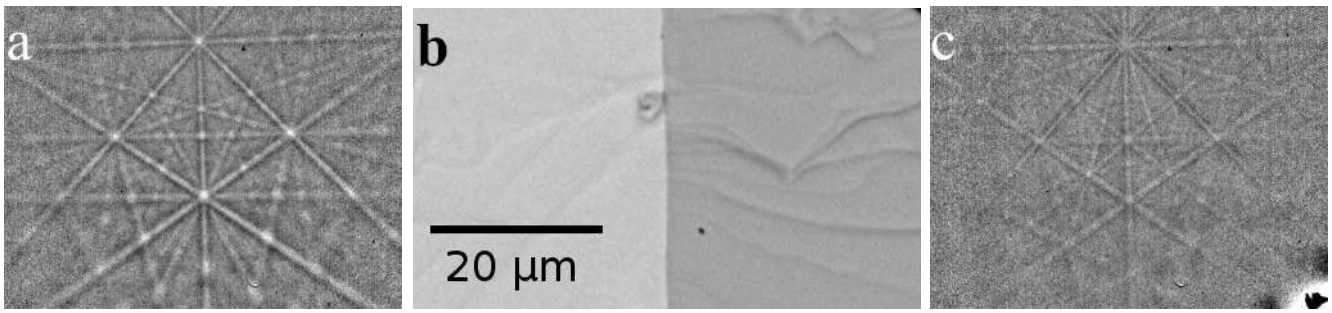

Figure 4.18 $CsPbBr_3/MAPbBr_3$ heterojunction on a single crystal cut: (a, c) EBSD patterns of the corresponding regions of $CsPbBr_3$ and $MAPbBr_3$, (b) BSE SEM of the $CsPbBr_3/MAPbBr_3$ heterojunction, heavier $CsPbBr_3$ is lighter

diffraction and high-resolution X-ray diffraction showed that the sample is a single-crystal with a unified orientation of the crystal axes despite differences in spatial groups and crystal cell constants (Figure 4.18).

The structure of the heterojunction was determined by photoelectron spectroscopy (UPS) at 10 K. The data obtained allow us to determine the VBM positions of the material and to conclude that the obtained heterointerface is a type 2 heterojunction (Figure 4.19). The position of the Fermi level agrees with the data on the high intrinsic hole conductivity of both semiconductors[15].

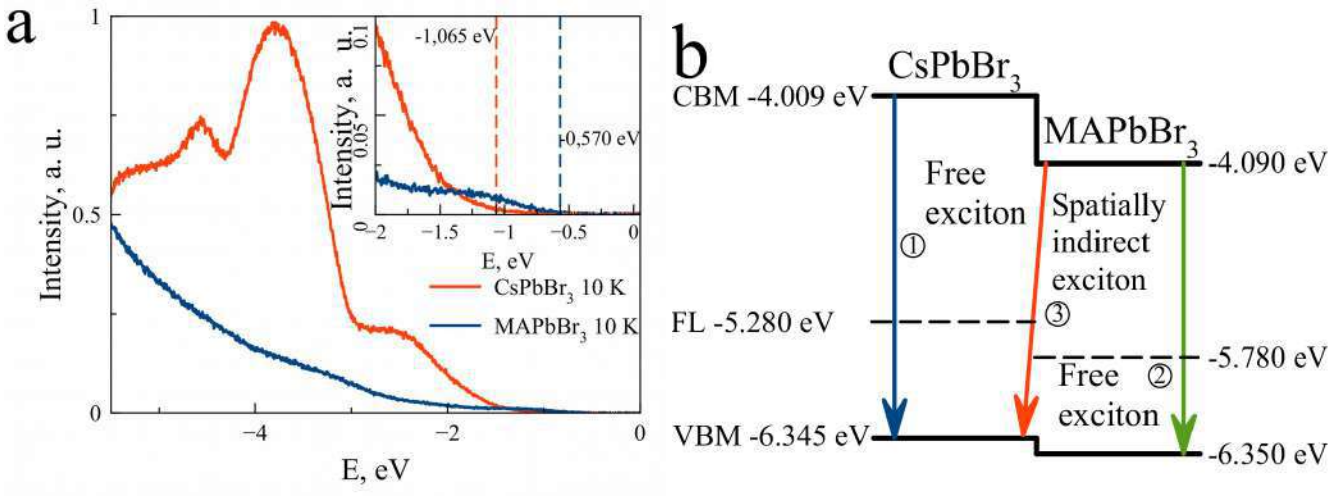

Figure 4.19 (a) 10 K UPS of $CsPbBr_3$ and $MAPbBr_3$ single crystals, VBM definition is on the insert, (b) heterojunction between $CsPbBr_3$ and $MAPbBr_3$ structure

For the heterojunctions of second type , it is possible to observe spatially indirect excitons formed by an electron of one material and a hole of another. In the

low-temperature crystal microphotoluminescence spectra, the spatially indirect exciton recombination peak observed near the interface is shifted to the red region relative to both materials (Figure 4.20), a shift that agrees well with UPS data. The free exciton peaks of the individual materials near the heterogeneous boundary have little broadening, which also indicates the high quality of the heterogeneous boundary. The

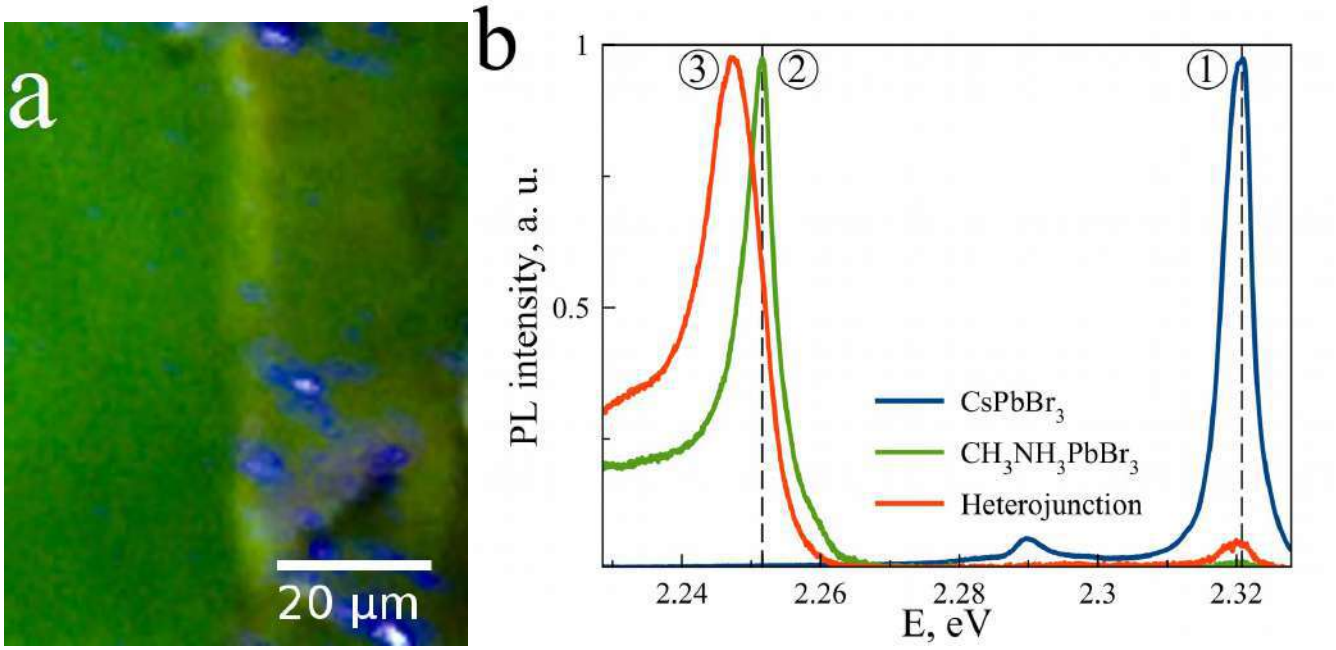

Figure 4.20 (a) PL of the $CsPbBr_3/MAPbBr_3$ heterointerface under 405 nm laser irradiation, (b) microphotoluminescence spectra in the region of pure $CsPbBr_3$ (1), $MAPbBr_3$ (2) and near the heterointerface (3)

possibility of observing a spatially indirect exciton is related to the high mobility of charge carriers and high quantum yield of the materials. The width of the PL indirect exciton peak is approximately twice the width of the bulk materials, we attribute this to the inhomogeneous broadening associated with the quality of the heterojunction and possible bands bending.

Conclusions

The main results of the work can be summarized as follows.

1. Monocrystals of $MAPbBr_3$, $CsPbBr_3$, $Cs_2AgBiBr_6$, and $MAPbI_3$ halide perovskites were studied. High-resolution low-temperature photoluminescence spectra were obtained for all materials. The photoluminescence data for halide perovskites are in good agreement with theoretical expectations on the ion substitution influence on the optical properties of crystals.
2. In the case of double perovskite, a resolved low-temperature photoluminescence spectrum containing three broad peaks corresponding to the three lowest transitions in the material L-X, G-X, and X-X according to theoretical modeling was obtained for the first time.
3. In the case of lead-based perovskites, the exciton binding energy values were obtained being in good agreement with the materials' bandgap bandgaps, in contrast to the common overestimation obtained in studies of powder samples[132;133].
4. In addition, for the first time for halide perovskites, resolved phonon replica lines corresponding to low-temperature Raman scattering frequencies are observed in low-temperature photoluminescence spectra.
5. The influence of the electron doping on the optical properties of the materials was studied and the theoretical assumption of the Fermi level shift and the absence of influence on the semiconductor band structure by heterovalent bismuth doping was confirmed by photoelectron spectroscopy.
6. $MAPbBr_3$/$CsPbBr_3$ monocrystal with the second type heterojunction was obtained by deposition from solution. In the low-temperature photoluminescence spectra, the spatially indirect exciton peak shifted to the red region. The value of the shift is in good agreement with photoelectron spectroscopy data.

Thus, this work proposes epitaxial pairs of halide perovskites for the growth of low dimentional structures in the optical range, studies the optical properties of individual materials and the possibility of control over their electrical properties, and demonstrates the fundamental possibility of obtaining heterostructures with abrupt interfaces based on halide perovskites.

Abbreviations

- **IR** – infrared
- **UV** – ultraviolet
- **BSE** – Backscattered electrons
- **CBM** – conduction band minimum
- **CCD** – charge-coupled device
- **DRS** – diffuse reflectance spectroscopy
- **EBSD** – backscattered electron diffrartion
- **EDX** – energy-dispersive X-ray spectroscopy
- **FA** – formamidinium, $NH_2CHNH_2^+$
- **FE** – free exciton
- **HWHM** – half width at half maximum
- **ICP-MS** – Inductively coupled plasma mass spectrometry
- **MA** – metylammonium, $CH_3NH_3^+$
- **PL** – photoluminescence
- **SRH** – Shockley-Read-Hall recombination
- **UPS** – ultraviolet photoelectron spectroscopy
- **VBM** – valence band maximum
- **WDS** – wavelength-dispersive X-ray spectroscopy
- **XPS** – X-ray photoelectron spectroscopy

Bibliography

1. *Lojek B.* History of Semiconductor Engineering [Text]. Berlin Heidelberg : Springer-Verlag GmbH, 2007.
2. *Alferov Z.* Heterostructures for Optoelectronics: History and Modern Trends [Text] // Proceedings of the IEEE. 2013. Vol. 101. P. 2176–2182.
3. *Rockett A.* The Materials Science of Semiconductors [Text]. US : Springer, 2008.
4. *Alferov Z. I.* Nobel Lecture: The double heterostructure concept and its applications in physics, electronics, and technology [Text] // Rev. Mod. Phys. 2001. Oct. Vol. 73, issue 3. P. 767–782.
5. *Cho A.*, *Arthur J.* Molecular beam epitaxy [Text] // Progress in Solid State Chemistry. 1975. Vol. 10. P. 157–191.
6. *Razeghi M.* Fundamentals of Solid State Engineering [Text]. US : Springer, 2009.
7. *Zhang B.*, *Liu Y.* A review of GaN-based optoelectronic devices on silicon substrate [Text] // Chinese Science Bulletin. 2014. Vol. 59. P. 1251–1275.
8. *Donaldson J.*, *Silver J.* High symmetry environments in compounds of elements with the ns2-outer-electronic configuration [Text] // Inorganic and Nuclear Chemistry Letters. 1974. Vol. 10, no. 7. P. 537–540.
9. *Clark S. J.*, *Flint C. D.*, *Donaldson J. D.* Luminescence and electrical conductivity of CsSnBr3, and related phases [Text] // Journal of Physics and Chemistry of Solids. 1981. Vol. 42, no. 3. P. 133–135.
10. *Heidrich K.*, *Künzel H.*, *Treusch J.* Optical properties and electronic structure of CsPbCl3 and CsPbBr3 [Text] // Solid State Communications. 1978. Vol. 25, no. 11. P. 887–889.
11. *Weber D.* CH3NH3PbX3, ein Pb(II)-System mit kubischer Perowskitstruktur / CH3NH3PbX3, a Pb(II)-System with Cubic Perovskite Structure [Text] // Zeitschrift für Naturforschung B. 1978. Vol. 33, no. 12. P. 1443–1445.
12. Novel Photoelectrochemical Cell with Mesoscopic Electrodes Sensitized by Lead-Halide Compounds (2) [Text] / A. Kojima [et al.] //. 2006.

13. Electron-hole diffusion lengths > 175 μm in solution-grown CH3NH3PbI3 single crystals [Text] / Q. Dong [et al.] // Science. 2015. Vol. 347, no. 6225. P. 967–970.

14. Organometal Halide Perovskite Solar Cell Materials Rationalized: Ultrafast Charge Generation, High and Microsecond-Long Balanced Mobilities, and Slow Recombination [Text] / C. S. Ponseca [et al.] // Journal of the American Chemical Society. 2014. Vol. 136, no. 14. P. 5189–5192.

15. Low trap-state density and long carrier diffusion in organolead trihalide perovskite single crystals [Text] / D. Shi [et al.] // Science. 2015. Vol. 347, no. 6221. P. 519–522.

16. Low Inhomogeneous Broadening of Excitonic Resonance in MAPbBr3 Single Crystals [Text] / O. A. Lozhkina [et al.] // The Journal of Physical Chemistry Letters. 2018. Vol. 9, no. 2. P. 302–305.

17. Historical Analysis of Champion Photovoltaic Module Efficiencies [Text] / S. Kurtz [et al.] // IEEE Journal of Photovoltaics. 2018. Vol. 8, no. 2. P. 363–372.

18. Enhancing photoluminescence yields in lead halide perovskites by photon recycling and light out-coupling [Text] / J. M. Richter [et al.] // Nature communications. 2016. Vol. 7, no. 1. P. 1–8.

19. Fabry–Pérot Oscillation and Room Temperature Lasing in Perovskite Cube-Corner Pyramid Cavities [Text] / Y. Mi [et al.] // Small. 2018. Vol. 14, no. 9. P. 1703136.

20. Green perovskite distributed feedback lasers [Text] / J. R. Harwell [et al.] // Scientific reports. 2017. Vol. 7, no. 1. P. 1–8.

21. Room-Temperature Red–Green–Blue Whispering-Gallery Mode Lasing and White-Light Emission from Cesium Lead Halide Perovskite (CsPbX3, X= Cl, Br, I) Microstructures [Text] / P. Guo [et al.] // Advanced Optical Materials. 2018. Vol. 6, no. 3. P. 1700993.

22. CsPbX3 nanocrystals films coated on YAG: Ce3+ PiG for warm white lighting source [Text] / S. Liu [et al.] // Chemical Engineering Journal. 2017. Vol. 330. P. 823–830.

23. Cs 2 AgBiBr 6 single-crystal X-ray detectors with a low detection limit [Text] / W. Pan [et al.] // Nature photonics. 2017. Vol. 11, no. 11. P. 726–732.

24. A self-powered and flexible organometallic halide perovskite photodetector with very high detectivity [Text] / S.-F. Leung [et al.] // Advanced Materials. 2018. Vol. 30, no. 8. P. 1704611.

25. Non-dissipative internal optical filtering with solution-grown perovskite single crystals for full-colour imaging [Text] / S. Yakunin [et al.] // NPG Asia Materials. 2017. Vol. 9, no. 9. e431–e431.

26. Structures, phase transitions and tricritical behavior of the hybrid perovskite methyl ammonium lead iodide [Text] / P. Whitfield [et al.] // Scientific reports. 2016. Vol. 6, no. 1. P. 1–16.

27. *Poglitsch A.*, *Weber D.* Dynamic disorder in methylammoniumtrihalogenoplumbates (II) observed by millimeter-wave spectroscopy [Text] // The Journal of chemical physics. 1987. Vol. 87, no. 11. P. 6373–6378.

28. Electronic structures of lead iodide based low-dimensional crystals [Text] / T. Umebayashi [et al.] // Physical Review B. 2003. Vol. 67, no. 15. P. 155405.

29. Defect tolerant semiconductors for solar energy conversion [Text] / A. Zakutayev [et al.] // The journal of physical chemistry letters. 2014. Vol. 5, no. 7. P. 1117–1125.

30. *Yin W.-J.*, *Shi T.*, *Yan Y.* Unique properties of halide perovskites as possible origins of the superior solar cell performance [Text] // Advanced Materials. 2014. Vol. 26, no. 27. P. 4653–4658.

31. *Tao S. X.*, *Cao X.*, *Bobbert P. A.* Accurate and efficient band gap predictions of metal halide perovskites using the DFT-1/2 method: GW accuracy with DFT expense [Text] // Scientific reports. 2017. Vol. 7, no. 1. P. 1–9.

32. *Gao P.*, *Grätzel M.*, *Nazeeruddin M. K.* Organohalide lead perovskites for photovoltaic applications [Text] // Energy & Environmental Science. 2014. Vol. 7, no. 8. P. 2448–2463.

33. Band gap tuning via lattice contraction and octahedral tilting in perovskite materials for photovoltaics [Text] / R. Prasanna [et al.] // Journal of the American Chemical Society. 2017. Vol. 139, no. 32. P. 11117–11124.

34. Origin of unusual bandgap shift and dual emission in organic-inorganic lead halide perovskites [Text] / M. I. Dar [et al.] // Science advances. 2016. Vol. 2, no. 10. e1601156.

35. *Fang H.*, *Jena P.* Super-ion inspired colorful hybrid perovskite solar cells [Text] // Journal of Materials Chemistry A. 2016. Vol. 4, no. 13. P. 4728–4737.

36. Cs2AgBiX6 (X= Br, Cl): new visible light absorbing, lead-free halide perovskite semiconductors [Text] / E. T. McClure [et al.] // Chemistry of Materials. 2016. Vol. 28, no. 5. P. 1348–1354.

37. Parity-forbidden transitions and their impact on the optical absorption properties of lead-free metal halide perovskites and double perovskites [Text] / W. Meng [et al.] // The journal of physical chemistry letters. 2017. Vol. 8, no. 13. P. 2999–3007.

38. Magnetic and Other Properties of Oxides and Related Compounds [Text] / J. Goodenough [et al.]. Berlin Heidelberg : Springer-Verlag GmbH, 1970.

39. Antagonism between Spin–Orbit Coupling and Steric Effects Causes Anomalous Band Gap Evolution in the Perovskite Photovoltaic Materials CH3NH3Sn1–x Pb x I3 [Text] / J. Im [et al.] // The journal of physical chemistry letters. 2015. Vol. 6, no. 17. P. 3503–3509.

40. Band-gap tuning of lead halide perovskites using a sequential deposition process [Text] / S. A. Kulkarni [et al.] // Journal of Materials Chemistry A. 2014. Vol. 2, no. 24. P. 9221–9225.

41. Structural, optical, and electronic studies of wide-bandgap lead halide perovskites [Text] / R. Comin [et al.] // Journal of Materials Chemistry C. 2015. Vol. 3, no. 34. P. 8839–8843.

42. Mixed cation hybrid lead halide perovskites with enhanced performance and stability [Text] / F. Xu [et al.] // Journal of Materials Chemistry A. 2017. Vol. 5, no. 23. P. 11450–11461.

43. Triple-cation mixed-halide perovskites: towards efficient, annealing-free and air-stable solar cells enabled by Pb (SCN) 2 additive [Text] / Y. Sun [et al.] // Scientific reports. 2017. Vol. 7, no. 1. P. 1–7.

44. Single crystals of caesium formamidinium lead halide perovskites: solution growth and gamma dosimetry [Text] / O. Nazarenko [et al.] // NPG Asia Materials. 2017. Vol. 9, no. 4. e373–e373.

45. Formability of ABX3 (X= F, Cl, Br, I) Halide Perovskites [Text] / C. Li [et al.] // Acta Crystallographica Section B: Structural Science. 2008. Vol. 64, no. 6. P. 702–707.

46. *Becker M.*, *Klüner T.*, *Wark M.* Formation of hybrid ABX 3 perovskite compounds for solar cell application: first-principles calculations of effective ionic radii and determination of tolerance factors [Text] // Dalton Transactions. 2017. Vol. 46, no. 11. P. 3500–3509.

47. *Shannon R. D.* Revised effective ionic radii and systematic studies of interatomic distances in halides and chalcogenides [Text] // Acta crystallographica section A: crystal physics, diffraction, theoretical and general crystallography. 1976. Vol. 32, no. 5. P. 751–767.

48. *Weber O.*, *Charles B.*, *Weller M.* Phase behaviour and composition in the formamidinium–methylammonium hybrid lead iodide perovskite solid solution [Text] // Journal of Materials Chemistry A. 2016. Vol. 4, no. 40. P. 15375–15382.

49. *Downs A.* Chemistry of Aluminium, Gallium, Indium and Thallium [Text]. Netherlands : Springer, 1993.

50. *Cox D.*, *Zawadowski A.* Exotic Kondo effects in metals: magnetic ions in a crystalline electric field and tunnelling centres [Text] // Advances in Physics. 1998. Vol. 47, no. 5. P. 599–942.

51. Ligand-hole in [SnI6] unit and origin of band gap in photovoltaic perovskite variant Cs2SnI6 [Text] / Z. Xiao [et al.] // Bulletin of the Chemical Society of Japan. 2015. Vol. 88, no. 9. P. 1250–1255.

52. High-efficiency rubidium-incorporated perovskite solar cells by gas quenching [Text] / M. Zhang [et al.] // ACS Energy Letters. 2017. Vol. 2, no. 2. P. 438–444.

53. Colloidal lead halide perovskite nanocrystals: synthesis, optical properties and applications [Text] / H. Huang [et al.] // NPG Asia Materials. 2016. Vol. 8, no. 11. e328–e328.

54. CH3NH3PbCl3 single crystals: inverse temperature crystallization and visible-blind UV-photodetector [Text] / G. Maculan [et al.] // The journal of physical chemistry letters. 2015. Vol. 6, no. 19. P. 3781–3786.

55. FAPbCl3 perovskite as alternative interfacial layer for highly efficient and stable polymer solar cells [Text] / J. Wang [et al.] // Advanced Electronic Materials. 2016. Vol. 2, no. 11. P. 1600329.

56. *Ding J.*, *Yan Q.* Progress in organic-inorganic hybrid halide perovskite single crystal: growth techniques and applications [Text] // Science China Materials. 2017. Vol. 60, no. 11. P. 1063–1078.

57. Ruddlesden–Popper hybrid lead iodide perovskite 2D homologous semiconductors [Text] / C. C. Stoumpos [et al.] // Chemistry of Materials. 2016. Vol. 28, no. 8. P. 2852–2867.

58. Layered 2D alkyldiammonium lead iodide perovskites: synthesis, characterization, and use in solar cells [Text] / M. Safdari [et al.] // Journal of Materials Chemistry A. 2016. Vol. 4, no. 40. P. 15638–15646.

59. *Baker R. J.*, *Jones C.* "GaI": A versatile reagent for the synthetic chemist [Text] // Dalton Transactions. 2005. No. 8. P. 1341–1348.

60. *B.K.Sharma*. Objective Pre Engineering Chemistry. Paperback [Text]. Meerut, India : Krishna prakashan, 2015.

61. Intrinsic instability of Cs2In (I) M (III) X6 (M= Bi, Sb; X= halogen) double perovskites: a combined density functional theory and experimental study [Text] / Z. Xiao [et al.] // Journal of the American Chemical Society. 2017. Vol. 139, no. 17. P. 6054–6057.

62. Lead-free organic–inorganic tin halide perovskites for photovoltaic applications [Text] / N. K. Noel [et al.] // Energy & Environmental Science. 2014. Vol. 7, no. 9. P. 3061–3068.

63. *Abate A.* Perovskite solar cells go lead free [Text] // Joule. 2017. Vol. 1, no. 4. P. 659–664.

64. *Toshniwal A.*, *Kheraj V.* Development of organic-inorganic tin halide perovskites: a review [Text] // Solar Energy. 2017. Vol. 149. P. 54–59.

65. *Huang L.-y.*, *Lambrecht W. R.* Electronic band structure, phonons, and exciton binding energies of halide perovskites CsSnCl 3, CsSnBr 3, and CsSnI 3 [Text] // Physical Review B. 2013. Vol. 88, no. 16. P. 165203.

66. Stabilizing the α-phase of CsPbI3 perovskite by sulfobetaine zwitterions in one-step spin-coating films [Text] / Q. Wang [et al.] // Joule. 2017. Vol. 1, no. 2. P. 371–382.

67. Tunable Band Gap and Long Carrier Recombination Lifetime of Stable Mixed CH3NH3Pb x Sn1–x Br3 Single Crystals [Text] / D. Ju [et al.] // Chemistry of Materials. 2018. Vol. 30, no. 5. P. 1556–1565.

68. Structure and Successive Phase Transitions of RGeBr3 (R= Alkylammonium) Studied by Means of NQR [Text] / T. Okuda [et al.] // ZEITSCHRIFT FUR NATURFORSCHUNG A. 1996. Vol. 51. P. 686–692.

69. Chloride ion conductor CH3NH3GeCl3 studied by Rietveld analysis of X-ray diffraction and 35Cl NMR [Text] / K. Yamada [et al.] // Solid State Ionics. 1995. Vol. 79. P. 152–157.

70. Hybrid germanium iodide perovskite semiconductors: active lone pairs, structural distortions, direct and indirect energy gaps, and strong nonlinear optical properties [Text] / C. C. Stoumpos [et al.] // Journal of the American Chemical Society. 2015. Vol. 137, no. 21. P. 6804–6819.

71. Lead-free mixed tin and germanium perovskites for photovoltaic application [Text] / M.-G. Ju [et al.] // Journal of the American Chemical Society. 2017. Vol. 139, no. 23. P. 8038–8043.

72. Exploring the properties of lead-free hybrid double perovskites using a combined computational-experimental approach [Text] / Z. Deng [et al.] // Journal of Materials Chemistry A. 2016. Vol. 4, no. 31. P. 12025–12029.

73. Route to stable lead-free double perovskites with the electronic structure of CH3NH3PbI3: a case for mixed-cation [Cs/CH3NH3/CH (NH2) 2] 2InBiBr6 [Text] / G. Volonakis [et al.] // The journal of physical chemistry letters. 2017. Vol. 8, no. 16. P. 3917–3924.

74. Bandgap engineering of lead-free double perovskite Cs2AgBiBr6 through trivalent metal alloying [Text] / K.-z. Du [et al.] // Angewandte Chemie International Edition. 2017. Vol. 56, no. 28. P. 8158–8162.

75. Halide-dependent electronic structure of organolead perovskite materials [Text] / A. Buin [et al.] // Chemistry of Materials. 2015. Vol. 27, no. 12. P. 4405–4412.

76. Excitonic emissions and above-band-gap luminescence in the single-crystal perovskite semiconductors CsPbB r 3 and CsPbC l 3 [Text] / M. Sebastian [et al.] // Physical Review B. 2015. Vol. 92, no. 23. P. 235210.

77. Defect Activity in Lead Halide Perovskites [Text] / S. G. Motti [et al.] // Advanced Materials. 2019. Vol. 31, no. 47. P. 1901183.

78. *Yin W.-J.*, *Shi T.*, *Yan Y.* Unusual defect physics in CH3NH3PbI3 perovskite solar cell absorber [Text] // Applied Physics Letters. 2014. Vol. 104, no. 6. P. 063903.

79. Efficient perovskite solar cells by metal ion doping [Text] / J. T.-W. Wang [et al.] // Energy & Environmental Science. 2016. Vol. 9, no. 9. P. 2892–2901.

80. N-type doping and energy states tuning in CH3NH3Pb1–x Sb2 x/3I3 perovskite solar cells [Text] / J. Zhang [et al.] // ACS Energy Letters. 2016. Vol. 1, no. 3. P. 535–541.

81. *Oku T.*, *Ohishi Y.*, *Suzuki A.* Effects of antimony addition to perovskite-type CH3NH3PbI3 photovoltaic devices [Text] // Chemistry Letters. 2016. Vol. 45, no. 2. P. 134–136.

82. Arsenic and chlorine co-doping to CH3NH3PbI3 perovskite solar cells [Text] / T. Hamatani [et al.] // Advances in Materials Physics and Chemistry. 2017. Vol. 7, no. 1. P. 1–10.

83. Fabrication and Characterization of Element-Doped Perovskite Solar Cells [Text] / T. Oku [et al.] // Nanostructured Solar Cells. 2017. P. 217–243.

84. Heterovalent dopant incorporation for bandgap and type engineering of perovskite crystals [Text] / A. L. Abdelhady [et al.] // The journal of physical chemistry letters. 2016. Vol. 7, no. 2. P. 295–301.

85. Enhanced optical absorption via cation doping hybrid lead iodine perovskites [Text] / Z.-K. Tang [et al.] // Scientific reports. 2017. Vol. 7, no. 1. P. 1–7.

86. *Timmermans C.*, *Blasse G.* The luminescence and photoconductivity of Cs3Bi2Br9 single crystals [Text] // Journal of Luminescence. 1981. Vol. 24. P. 75–78.

87. Bandgap narrowing in Bi-doped CH3NH3PbCl3 perovskite single crystals and thin films [Text] / Z. Zhang [et al.] // The Journal of Physical Chemistry C. 2017. Vol. 121, no. 32. P. 17436–17441.

88. Bi3+-doped CH3NH3PbI3: Red-shifting absorption edge and longer charge carrier lifetime [Text] / R. Wang [et al.] // Journal of Alloys and Compounds. 2017. Vol. 695. P. 555–560.

89. Air-stable CsPb 1- x Bi x Br 3 (0≤ x□ 1) perovskite crystals: optoelectronic and photostriction properties [Text] / X. Miao [et al.] // Journal of Materials Chemistry C. 2017. Vol. 5, no. 20. P. 4931–4939.

90. Impact of chemical doping on optical responses in bismuth-doped CH3NH3PbBr3 single crystals: carrier lifetime and photon recycling [Text] / Y. Yamada [et al.] // The journal of physical chemistry letters. 2017. Vol. 8, no. 23. P. 5798–5803.

91. Impact of Bi3+ heterovalent doping in organic–inorganic metal halide perovskite crystals [Text] / P. K. Nayak [et al.] // Journal of the American Chemical Society. 2018. Vol. 140, no. 2. P. 574–577.

92. Long minority-carrier diffusion length and low surface-recombination velocity in inorganic lead-free CsSnI3 perovskite crystal for solar cells [Text] / B. Wu [et al.] // Advanced Functional Materials. 2017. Vol. 27, no. 7. P. 1604818.

93. *Scaife D. E.*, *Weller P. F.*, *Fisher W. G.* Crystal preparation and properties of cesium tin (II) trihalides [Text] // Journal of Solid State Chemistry. 1974. Vol. 9, no. 3. P. 308–314.

94. Formation of hybrid perovskite tin iodide single crystals by top-seeded solution growth [Text] / Y. Dang [et al.] // Angewandte Chemie International Edition. 2016. Vol. 55, no. 10. P. 3447–3450.

95. Retrograde solubility of formamidinium and methylammonium lead halide perovskites enabling rapid single crystal growth [Text] / M. I. Saidaminov [et al.] // Chemical communications. 2015. Vol. 51, no. 100. P. 17658–17661.

96. Understanding the cubic phase stabilization and crystallization kinetics in mixed cations and halides perovskite single crystals [Text] / L.-Q. Xie [et al.] // Journal of the American Chemical Society. 2017. Vol. 139, no. 9. P. 3320–3323.

97. A formamidinium–methylammonium lead iodide perovskite single crystal exhibiting exceptional optoelectronic properties and long-term stability [Text] / W.-G. Li [et al.] // Journal of Materials Chemistry A. 2017. Vol. 5, no. 36. P. 19431–19438.

98. Highly narrowband perovskite single-crystal photodetectors enabled by surface-charge recombination [Text] / Y. Fang [et al.] // Nature Photonics. 2015. Vol. 9, no. 10. P. 679–686.

99. Structure and growth control of organic–inorganic halide perovskites for optoelectronics: From polycrystalline films to single crystals [Text] / Y. Chen [et al.] // Advanced Science. 2016. Vol. 3, no. 4. P. 1500392.

100. High-Temperature Ionic Epitaxy of Halide Perovskite Thin Film and the Hidden Carrier Dynamics [Text] / Y. Wang [et al.] // Advanced Materials. 2017. Vol. 29, no. 35. P. 1702643.

101. NMR study of ionic conduction in the perovskite-type halides [Text] / T. Kanashiro [et al.] // Defects in insulating materials. Proceedings of the XII International Conference. 1992.

102. Formation of perovskite heterostructures by ion exchange [Text] / N. T. Shewmon [et al.] // ACS applied materials & interfaces. 2016. Vol. 8, no. 48. P. 33273–33279.

103. An optical dynamic study of MAPbBr 3 single crystals passivated with MAPbCl 3/I 3-MAPbBr 3 heterojunctions [Text] / H. Lu [et al.] // Physical Chemistry Chemical Physics. 2017. Vol. 19, no. 6. P. 4516–4521.

104. High-Performance Photodetectors Based on Solution-Processed Epitaxial Grown Hybrid Halide Perovskites [Text] / L. Ji [et al.] // Nano Letters. 2018. Vol. 18, no. 2. P. 994–1000.

105. Epitaxial halide perovskite lateral double heterostructure [Text] / Y. Wang [et al.] // ACS nano. 2017. Vol. 11, no. 3. P. 3355–3364.

106. Carrier lifetime enhancement in halide perovskite via remote epitaxy [Text] / J. Jiang [et al.] // Nature communications. 2019. Vol. 10, no. 1. P. 1–12.

107. Wide band-gap tuning in Sn-based hybrid perovskites through cation replacement: the FA 1- x MA x SnBr 3 mixed system [Text] / C. Ferrara [et al.] // Journal of Materials Chemistry A. 2017. Vol. 5, no. 19. P. 9391–9395.

108. Anomalous band gap behavior in mixed Sn and Pb perovskites enables broadening of absorption spectrum in solar cells [Text] / F. Hao [et al.] // Journal of the American Chemical Society. 2014. Vol. 136, no. 22. P. 8094–8099.

109. Perovskite FA1-xMAxPbI3 for solar cells: films formation and properties [Text] / B. Slimi [et al.] // Energy Procedia. 2016. Vol. 102. P. 87–95.

110. *Davey W. P.* Precision measurements of crystals of the alkali halides [Text] // Physical Review. 1923. Vol. 21, no. 2. P. 143.

111. *Linaburg M. R.* Studies of Halide Perovskites CsPbX 3, RbPbX 3 (X= Cl-, Br-, I-), and Their Solid Solutions [Text] : PhD thesis / Linaburg Matthew Ronald. The Ohio State University, 2015.

112. *П.К.Кашкаров*, *Тимошенко В.* Оптика твердого тела и систем пониженной размерности [Text]. Москва : Пульс, 2008.

113. *Lee J.*, *Koteles E. S.*, *Vassell M.* Luminescence linewidths of excitons in GaAs quantum wells below 150 K [Text] // Physical Review B. 1986. Vol. 33, no. 8. P. 5512.

114. *Агекян В.*, *Григорьева Н.* Люминесценция полупроводниковых кристаллов [Text]. Санкт-Петербург : СПбГУ, 2016.

115. High detectivity and rapid response in perovskite CsPbBr3 single-crystal photodetector [Text] / J. Ding [et al.] // The Journal of Physical Chemistry C. 2017. Vol. 121, no. 9. P. 4917–4923.

116. Band gaps of the lead-free halide double perovskites Cs2BiAgCl6 and Cs2BiAgBr6 from theory and experiment [Text] / M. R. Filip [et al.] // The journal of physical chemistry letters. 2016. Vol. 7, no. 13. P. 2579–2585.

117. Wikipedia The Free Encyclopedia [Text]. `https://en.wikipedia.org/`.

118. Microstructural analysis and optical properties of the halide double perovskite Cs2BiAgBr6 single crystals [Text] / O. Lozhkina [et al.] // Chemical Physics Letters. 2018. Vol. 694. P. 18–22.

119. *Miyata K.*, *Atallah T. L.*, *Zhu X.-Y.* Lead halide perovskites: Crystal-liquid duality, phonon glass electron crystals, and large polaron formation [Text] // Science Advances. 2017. Vol. 3, no. 10. e1701469.

120. Quantification of re-absorption and re-emission processes to determine photon recycling efficiency in perovskite single crystals [Text] / Y. Fang [et al.] // Nature communications. 2017. Vol. 8, no. 1. P. 1–9.

121. Role of the A-Site Cation in Low-Temperature Optical Behaviors of APbBr3 (A = Cs, CH3NH3) [Text] / H. Ryu [et al.] // Journal of the American Chemical Society. 2021. Vol. 143, no. 5. P. 2340–2347.

122. Hydrogen-like Wannier–Mott excitons in single crystal of methylammonium lead bromide perovskite [Text] / J. Tilchin [et al.] // ACS nano. 2016. Vol. 10, no. 6. P. 6363–6371.

123. Nonlinear carrier interactions in lead halide perovskites and the role of defects [Text] / A. R. Srimath Kandada [et al.] // Journal of the American Chemical Society. 2016. Vol. 138, no. 41. P. 13604–13611.

124. *Varshni Y. P.* Temperature dependence of the energy gap in semiconductors [Text] // physica. 1967. Vol. 34, no. 1. P. 149–154.

125. Extremely low inhomogeneous broadening of exciton lines in shallow (In, Ga) As/GaAs quantum wells [Text] / S. Poltavtsev [et al.] // Solid state communications. 2014. Vol. 199. P. 47–51.

126. *Haug H.*, *Koch S. W.* Quantum theory of the optical and electronic properties of semiconductors [Text]. World Scientific Publishing Company, 2009.

127. Lattice dynamics and vibrational spectra of the orthorhombic, tetragonal, and cubic phases of methylammonium lead iodide [Text] / F. Brivio [et al.] // Physical Review B. 2015. Vol. 92, no. 14. P. 144308.

128. Local polar fluctuations in lead halide perovskite crystals [Text] / O. Yaffe [et al.] // Physical review letters. 2017. Vol. 118, no. 13. P. 136001.

129. Identification of the symmetry of phonon modes in CsPbCl 3 in phase IV by Raman and resonance-Raman scattering [Text] / D. M. Calistru [et al.] // Journal of applied physics. 1997. Vol. 82, no. 11. P. 5391–5395.

130. Invalidity of Band-Gap Engineering Concept for Bi3+ Heterovalent Doping in CsPbBr3 Halide Perovskite [Text] / O. A. Lozhkina [et al.] // The journal of physical chemistry letters. 2018. Vol. 9, no. 18. P. 5408–5411.

131. Effect of bismuth substitution for lead in CsPbBr3 perovskite [Text] / M. Elizarov [et al.] // Journal of Physics: Conference Series. Vol. 993. IOP Publishing. 2018. P. 012004.

132. Absorption F-sum rule for the exciton binding energy in methylammonium lead halide perovskites [Text] / N. Sestu [et al.] // The journal of physical chemistry letters. 2015. Vol. 6, no. 22. P. 4566–4572.

133. *Wolf C.*, *Lee T.-W.* Exciton and lattice dynamics in low-temperature processable CsPbBr3 thin-films [Text] // Materials today energy. 2018. Vol. 7. P. 199–207.

List of figures

List of tables

Appendix A

Octahedral factors μ and tolerance factors τ for B cations with lone-pairs on the valence *s*-orbital

Calculated values of the octahedral factors μ and tolerance factors τ for B cations with lone-pairs on the valence *s*-orbital; values predicting stable and unstable compounds are highlighted in green and red, respectively

Formula	μ	τ	Formula	μ	τ	Formula	μ	τ
Ge^{2+}			Ga^{+}			As^{3+}		
$RbGeCl_3$	0,403	0,983	$[RbGaCl_3]^-$	0,624	0,849	$[RbAsCl_3]^+$	0,320	1,045
$RbGeBr_3$	0,372	0,967	$[RbGaBr_3]^-$	0,574	0,842	$[RbAsBr_3]^+$	0,296	1,025
$RbGeI_3$	0,332	0,946	$[RbGaI_3]^-$	0,514	0,833	$[RbAsI_3]^+$	0,264	0,997
$CsGeCl_3$	0,403	1,027	$[CsGaCl_3]^-$	0,624	0,888	$[CsAsCl_3]^+$	0,320	1,092
$CsGeBr_3$	0,372	1,010	$[CsGaBr_3]^-$	0,574	0,879	$[CsAsBr_3]^+$	0,296	1,069
$CsGeI_3$	0,332	0,985	$[CsGaI_3]^-$	0,514	0,866	$[CsAsI_3]^+$	0,264	1,038
$MAGeCl_3$	0,403	1,108	$[MAGaCl_3]^-$	0,624	0,957	$[MAAsCl_3]^+$	0,320	1,178
$MAGeBr_3$	0,372	1,086	$[MAGaBr_3]^-$	0,574	0,945	$[MAAsBr_3]^+$	0,296	1,150
$MAGeI_3$	0,332	1,054	$[MAGaI_3]^-$	0,514	0,928	$[MAAsI_3]^+$	0,264	1,112
$FAGeCl_3$	0,403	1,208	$[FAGaCl_3]^-$	0,624	1,044	$[FAAsCl_3]^+$	0,320	1,284
$FAGeBr_3$	0,372	1,180	$[FAGaBr_3]^-$	0,574	1,028	$[FAAsBr_3]^+$	0,296	1,250
$FAGeI_3$	0,332	1,142	$[FAGaI_3]^-$	0,514	1,005	$[FAAsI_3]^+$	0,264	1,203
Sn^{2+}			In^{+}			Sb^{3+}		
$RbSnCl_3$	0,514	0,911	$[RbInCl_3]^-$	0,729	0,798	$[RbSbCl_3]^+$	0,420	0,971
$RbSnBr_3$	0,474	0,901	$[RbInBr_3]^-$	0,673	0,793	$[RbSbBr_3]^+$	0,388	0,957
$RbSnI_3$	0,423	0,886	$[RbInI_3]^-$	0,600	0,788	$[RbSbI_3]^+$	0,345	0,937
$CsSnCl_3$	0,514	0,952	$[CsInCl_3]^-$	0,729	0,834	$[CsSbCl_3]^+$	0,420	1,015
$CsSnBr_3$	0,474	0,940	$[CsInBr_3]^-$	0,673	0,828	$[CsSbBr_3]^+$	0,388	0,998
$CsSnI_3$	0,423	0,922	$[CsInI_3]^-$	0,600	0,820	$[CsSbI_3]^+$	0,345	0,975
$MASnCl_3$	0,514	1,027	$[MAInCl_3]^-$	0,729	0,899	$[MASbCl_3]^+$	0,420	1,095
$MASnBr_3$	0,474	1,011	$[MAInBr_3]^-$	0,673	0,890	$[MASbBr_3]^+$	0,388	1,074
$MASnI_3$	0,423	0,987	$[MAInI_3]^-$	0,600	0,878	$[MASbI_3]^+$	0,345	1,044
$FASnCl_3$	0,514	1,120	$[FAInCl_3]^-$	0,729	0,981	$[FASbCl_3]^+$	0,420	1,194
$FASnBr_3$	0,474	1,099	$[FAInBr_3]^-$	0,673	0,968	$[FASbBr_3]^+$	0,388	1,167
$FASnI_3$	0,423	1,069	$[FAInI_3]^-$	0,600	0,950	$[FASbI_3]^+$	0,345	1,130
Pb^{2+}			Tl^{+}			Bi^{3+}		
$RbPbCl_3$	0,657	0,832	$[RbTlCl_3]^-$	0,829	0,754	$[RbBiCl_3]^+$	0,569	0,879
$RbPbBr_3$	0,607	0,826	$[RbTlBr_3]^-$	0,705	0,752	$[RbBiBr_3]^+$	0,526	0,870
$RbPbI_3$	0,541	0,818	$[RbTlI_3]^-$	0,682	0,749	$[RbBiI_3]^+$	0,468	0,858
$CsPbCl_3$	0,657	0,870	$[CsTlCl_3]^-$	0,829	0,788	$[CsBiCl_3]^+$	0,569	0,919
$CsPbBr_3$	0,607	0,862	$[CsTlBr_3]^-$	0,705	0,785	$[CsBiBr_3]^+$	0,526	0,908
$CsPbI_3$	0,541	0,851	$[CsTlI_3]^-$	0,682	0,780	$[CsBiI_3]^+$	0,468	0,893
$MAPbCl_3$	0,657	0,938	$[MATlCl_3]^-$	0,829	0,850	$[MABiCl_3]^+$	0,569	0,991

Appendix B

List of materials and reagents used for synthesis

- MABr, chemically pure
- CsBr, chemically pure
- $PbBr_2$, chemically pure
- AgBr, chemically pure
- $BiBr_3$, chemically pure
- Dimethylformamide, high purity
- Dimethylsulfoxide, high purity
- Bromic acid, 48% pure
- Ethanol, 95% pure
- Distilled water
- Laboratory analytical balance, accuracy class I, resolution 0.0001 g
- Magnetic stirrer with heating ceramic surface
- Leica M205 polarizing optical stereomicroscope
- Metal spatulas
- Laboratory pipettes of variable volume of 2-20, 10-100 and 100-1000 μl
- 5 ml pipettes with pipetator
- 10ml volumetric flasks, accuracy class 2
- Glass funnels, d=36mm
- 20 and 100 mL laboratory glass beakers
- Glass beakers 100ml
- Syringe cellulose filters, 0,2μm pore diameter
- Anatomical forceps 125mm
- Surgical scalpel
- 2 ml disposable eppendorf tubes
- Tapered disposable conical tubes with screw cap 10 ml